Received 00th January 20xx,
Accepted 00th January 20xx

DOI: 10.1039/x0xx00000x

The electronic properties of three popular high spin complexes [TM(acac)$_3$, TM= Cr, Mn, and Fe] revisited: an experimental and theoretical study.†

S. Carlotto,*[a] L. Floreano,[b] A. Cossaro,[b] M. Dominguez,[b,c] M. Rancan,[d] M. Sambi,[a] M. Casarin*[a,d]

The occupied and unoccupied electronic structure of three high spin TM(acac)$_3$ (TM = Cr, Mn, and Fe) complexes (**I**, **II**, and **III**, respectively) has been studied by revisiting their literature vapour-phase He(I) and, when available, He(II) photoemission (PE) spectra and by means of original near-edge X-ray absorption fine structure (NEXAFS) spectroscopic data recorded at the O K-edge (^{O}K-edge) and TM $L_{2,3}$-edges ($^{TM}L_{2,3}$-edges). The assignments of the vapour-phase He(I)/He(II) PE spectra have been guided by the results of spin-unrestricted non-relativistic Slater transition state calculations, while the ^{O}K-edge and $^{TM}L_{2,3}$-edges spectroscopic evidences have been analysed by exploiting the results of spin-unrestricted scalar-relativistic time-dependent density funtional theory (DFT) and DFT/ROCIS calculations, respectively. Despite the actual symmetry (D_3, in the absence of any Jahn-Teller distorsion) of title molecules allows an extensive mixing between TM t_{2g}-like and e_g-like atomic orbitals, the use of the Nalewajski–Mrozek TM–O bond multiplicity index combined to a thorough analysis of the ground state (GS) outcomes allowed the assessment of the TM–O bond weakening associated to the progressive TM 3d-based e_g-like orbitals filling. The experimental information provided by ^{O}K-edge spectra was rather poor; nevertheless, the combined use of symmetry, orbitals and spectra allowed us: i) to rationalise minor differences characterizing spectral features along the series; ii) to quantify the contribution provided by the ligand-to-metal-charge-tranfer (LMCT) excitations to the differet spectral features; iii) to recognize the t_{2g}-/e_g-like nature of the TM 3d-based orbitals involved in LMCT transitions. As far as the $^{TM}L_{2,3}$-edges spectra and the DFT/ROCIS results are concerned, lowest lying $^{I,II}L_3$ spectral features include states having either the GS spin multiplicity (S(**I**) = 3/2, S(**II**) = 2) or, at higher excitation energies (*EE*s), states with $\Delta S = \pm 1$. At variance to that, only states with $\Delta S = 0, -1$ significantly contribute to the $^{III}L_3$ spectral pattern. Along the whole series, the L_3 higher *EE* side is systematically characterized by states involving $^{TM}2p \rightarrow \pi_4$ MLCT excitations; as such, coupled-single excitations with $\Delta S = 0$ are involved in **I** and **II**, while single MLCT $^{TM}2p \rightarrow \pi_4$ transitions with $\Delta S = -1$ are involved in **III**.

1. Introduction

The pentane-2,4-dione, commonly addressed as acetylacetone, is the simplest member of the β-diketone compounds and the precursor of one of the most prominent and versatile ligand (L) in coordination chemistry: the bidentate, negatively charged, acetylacetonato (acac).[1] Acac may bind to transition metal (TM) ions in different ways;[2] nevertheless, the bidentate chelating form, with both O atoms bound to TM to generate a six-membered pseudoaromatic ring,[3] is by far the most common.[2,4] TM(acac)$_n$ complexes usually imply n = 2 or n = 3, with TM(acac)$_2$ quite often oligomeric to allow the TM coordinative saturation, and TM(acac)$_3$ characterized by an *octahedral* arrangement of the six O atoms around TM (see Fig. 1).[5-6] Among TM(acac)$_3$, the peculiar properties of the high spin (HS) Cr(acac)$_3$, Mn(acac)$_3$ and Fe(acac)$_3$ (**I**, **II**, and **III**, respectively) make them interesting for both basic and applied research.[7-9] More specifically, besides its *martial* uses,[10] the deep maroon **I** is extensively used as a precursor in plasma assisted Chemical Vapour Deposition (CVD)[9a] and as a dopant agent in sol-gel silica films.[9b] Moreover, in the last few years, it has been employed as a general precursor for the synthesis of early TM oxide nanomaterials and nanoparticles[11-12] as well as redox species of redox flow batteries.[13-16] Furthermore, its high degree of photostability makes it the prototype Cr^{III} complex for ultrafast time-resolved spectroscopic studies.[17]

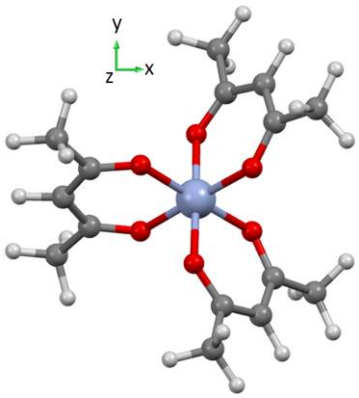

Fig. 1 Schematic representation of TM(acac)$_3$. The central violet sphere corresponds to the TM^{III} ion (Cr^{III} in **I**, Mn^{III} in **II**, and Fe^{III} in **III**), while red, grey,

[a] *Dipartimento di Scienze Chimiche, Università degli Studi di Padova, Via Francesco Marzolo 1, I-35131 Padova (Italy). E-mail: maurizio.casarin@unipd.it, silvia.carlotto@unipd.it.*
[b] *CNR-IOM, Laboratorio TASC, Basovizza S.S. 14, Km 163.5, I-34149 Trieste* (Italy).
[c] *Dipartimento di Fisica, Università degli Studi di Trieste, Via Alfonso Valerio 2, I-34127 Trieste (Italy).*
[d] *Istituto di Chimica della Materia Condensata e di Tecnologie per l'Energia - ICMATE, Via Francesco Marzolo 1, I-35131 Padova (Italy).*

†Electronic supplementary information (ESI) available: Fig. S1: Spin-unrestricted scalar relativistic ZORA TD-DFT $1s^{O}$ excitation spectra of Cr(acac)$_3$ evaluated with diverse exchange-correlations functionals: SAOP, LB94, PBE0 and M06; Fig. S2: Spin ↑ and spin ↓ COOPs between TM^{III} e_g-like 3d AOs and the e linear combination of the $(acac)_3^{3-}$-based n^- and n^+ fragment molecular orbitals.; Fig. S3: Superimposed licorice representation of title compounds; Table S1: TM–O Nalewajski–Mrozek index, Hirshfeld/Voronoi charges and bonding energies; Table S2: Comparison between experimental and theoretical ionization energies of the highest occupied molecular orbital in title compounds; Table S3: Selected optimized geometrical parameters for title compounds; Tables S4–S6: DFT-BP86 optimized coordinates of title compounds; Tables S7–S9: Excitation energies and oscillator strengths *f* of the $1s^{O}$ excitation spectra of TM(acac)$_3$ (TM = Cr, Mn, Fe) from spin-unrestricted SR-ZORA TD-DFT calculations.

and white spheres represent oxygen, carbon, and hydrogen atoms, respectively. In the adopted framework, *z* and C_3 axes coincide.

As far as the dark black-brown **II** is concerned, it has been the object of several theoretical[8d,18] and experimental[18c,19] studies, which ultimately demonstrated the Mn^{III} *octahedral* local environment[19a,b] as well as its HS state.[7,19c] Moreover, its effectiveness as a radical initiator and a hydroperoxide decomposition catalyst has been exploited in the autoxidation of ethyl linoleate, a model compound for the binder molecule in household alkyd paint.[20] The last $TM(acac)_3$ herein considered, the bright red HS **III**,[7-8] is widely employed in industry as a catalyst, in particular in the organic synthesis of alkenes[21] and polyurethane.[22] Additionally, it has been also found effective in catalytic processes such as the polymerization of 1,3-benzoxazine,[23] the dimerization of isoprene to 1,5-dimethyl-1,5-cyclooctadiene and 2,5-dimethyl-1,5-cyclooctadiene,[24] and the formation of 1,3-oxazolidine products.[25] More recently, **III** has been also exploited as precursor for nanoparticles' syntheses,[26] while an electrolyte based on the neutral/negatively charged (-1) **III** has been recently developed for p-type dye-sensitized solar cells.[27]

Despite the very large amount of literature concerning title compounds, a comparative assessment of their TM–L bonding scheme by taking advantage of peculiarities such as i) the same *octahedral* coordinative environment of the TM ion, ii) the same oxidation number of the TM ion, iii) the same number of $^{TM}t_{2g}$-like electrons,[5,7] and iv) the progressive increasing of the $^{TM}e_g$-like electron number,[5,7] is still lacking. Furthermore, it is noteworthy that not only a definitive assignment of the vapour-phase UV photoemission (PE) spectra of **I** – **III**[28] is still missing, but the same relative energy ordering of corresponding ground state (GS) occupied frontier molecular orbitals (MOs)[8h,29-31] deserves to be reconsidered.

Near edge X-ray absorption fine structure (NEXAFS) spectroscopy is unanimously recognized as a tool able to probe, site-selectively, the empty frontier MOs, the TM coordinative environment, as well as the nature and the strength of the TM–L bonding in TM complexes.[32-34] In the recent past, we thoroughly investigated the nature, the localization and the relative position of frontier MOs of three $TM(acac)_2$ complexes, namely $[Co(acac)_2]$,[35a] $[Mn(acac)_2]$,[35] and $[Cu(acac)_2]$,[36] by modelling their $^{TM}L_{2,3}$-edges spectra[37] either by employing the current Restricted Open Shell Configuration Interaction with Singles (DFT/ROCIS) method[38] ($[Co(acac)_2]$ and $[Mn(acac)_2]$) or by means of time dependent (TD) density functional theory (DFT) calculations[39] within the Tamm–Dancoff approximation[40] coupled to the relativistic zeroth-order regular approximation (ZORA)[41] including spin-orbit coupling (SOC) effects ($[Cu(acac)_2]$). The main aim of these studies was that of looking into the role played by the TM electronic configuration, the TM coordinative geometry, and the TM–L symmetry restricted covalency[42] in determining the $^{TM}L_{2,3}$ spectral patterns. ^{O}K-edge, $^{TM}L_{2,3}$-edges data and theoretical results herein reported complement experimental[17,29] and theoretical outcomes[8c-8h,43] appeared in the literature in the last few years about title compounds shedding, at the same time, new light into the TM–L bonding scheme and suggesting an alternative assignment of the lowest ionization energy (IE) region of their literature vapour-phase He(I) PE spectra.

2. Computational and Experimental Details

2.1 Geometry optimizations. Geometrical parameters of **I**, **II**, and **III** have been optimized by using the Amsterdam Density Functional (ADF) suite of programs (version 2014.01).[44] Numerical experiments have been carried out by running spin-unrestricted non-relativistic (NR) DFT calculations with generalized gradient corrections self-consistently included through the Becke-Perdew formula[45] and by adopting a triple-ζ with a polarization function (TZP) Slater-type basis set for all the atoms. Moreover, the 1s – 2p TM atomic orbitals (AOs) as well as the 1s AO of C and O atoms have been kept frozen throughout the calculations. The geometry optimization of **I** and **III** has been carried out by assuming a D_3 symmetry,[5,46] while no symmetry constraint has been assumed for **II**. As a matter of fact, X-ray crystallographic data pertaining to **II** are consistent with the presence of two crystal structures (β and γ), the former characterized by a moderate (0.05 Å) tetragonal compression,[19a] the latter typified by a significant tetragonal lengthening (0.2 Å).[19b-c] In this regard, Krzystek *et al.*,[19c] on the basis of their EPR measurements, suggested that the elongated γ structure is the natural form of the Jahn-Teller distortion for the *octahedral* HS $3d^4$ Mn^{III} ions, while the compressed β one could be the consequence of undetermined crystal packing effects. In passing, theoretical calculations confirmed the stabilizing effect associated to the Jahn-Teller elongation or predicted a stable elongated structure.[18] According to that and independently of the starting geometry we assumed (tetragonally elongated or compressed), the optimized structure of **II** systematically converged toward the same elongated arrangement. More specifically, the observed Jahn-Teller tetragonal distortion generating four short and two long Mn–O bonds ($(Mn–O)^s$ and $(Mn–O)^l$, respectively) with average bond lengths of 1.935 and 2.111 Å, respectively,[19] has been quantitatively reproduced irrespective of the starting geometry. Independently of all this, to facilitate the comparative assessment of the TM–L bonding and to assign ^{O}K-edge and $L_{2,3}$-edges features as seamless as possible, the electronic properties of title molecules will be discussed within the assumption of a D_3 symmetry and by taking advantage of the TM local *octahedral* environment.[5,46] Additional information about the localization and the bonding/antibonding character of selected MOs over a broad range of energies has been gained by exploiting partial density of states (PDOS) and the overlap population DOS (often referred to as crystal orbital overlap population – COOP).[48] Corresponding plots, based on the Mulliken's prescription for partitioning the overlap density,[49] have been obtained by applying a 0.25 eV Lorentzian broadening factor. Finally, the Ziegler transition state (^{Z}TS) scheme[50] has been used to gain further insights into the strength of the TM–L interaction.

2.2 O K-edge NEXAFS calculations.[51] O K-edge NEXAFS spectra of **I**, **II** and **III** have been modelled by evaluating *EE*s and corresponding oscillator strengths (*f*) for transitions having the linear combinations of $1s^O$ AOs as initial spin orbitals (isos).[62] To this end, all-electron spin-unrestricted scalar relativistic (SR) TD-DFT ZORA calculations[39,41] suitably tailored to treat deep core excitations,[63] have been run. SR TD-DFT ZORA numerical experiments have been carried out by adopting all-electron quadruple-ζ plus four polarization functions (QZ4P) ZORA basis sets for all the atoms;[64] moreover, to adequately describe transitions towards high energy virtual MOs and Rydberg states,[63] QZ4P ZORA sets of symmetry-related atoms specifically involved in the excitation processes have been further augmented with two shells of diffuse functions according to the even tempered criterion. The adiabatic local density approximation has been employed to approximate the exchange-correlation (XC) kernel,[65] while diverse functionals (PBE0,[66] SAOP,[67] LB94,[68] and M06[69]) have been preliminary tested on **I** to approximate the XC potential in the self-consistent field calculations. The best agreement between theory and experiment has been provided by the PBE0 functional (^{I}f distributions evaluated with PBE0,[66] SAOP,[67] LB94[68] and M06[69] XC functionals are displayed in Fig. S1);[70] ^{II}f and ^{III}f distributions have been then obtained by considering only the PBE0[66] XC functional. Scaled ZORA orbital energies instead of the ZORA orbital energies in the TD-DFT equations have been employed to improve deep core *EE*s.[63c-63e, 63g,71]

2.3 TM $L_{2,3}$-edges NEXAFS calculations.[51] $L_{2,3}$-edges spectra of **I**, **II** and **III** have been modelled by evaluating *EE*s and corresponding *f* for transitions having the ^{TM}2p-based MOs as isos. To this end, the ORCA program package[38] has been exploited. More specifically, $L_{2,3}$-edges $^{I/II/III}f(EE)$ distributions have been evaluated by means of the DFT/ROCIS method,[57c,57g] by adopting the hybrid-DFT PBE0 XC functional and the def2-TZVP(-f) basis set.[72-73] As a consequence of the strong 2p SOC in the final state manifold, ESs with S[46] different from the GS one had to be considered. The combined use of DFT and CI needs a set of three semi-empirical parameters (c_1, c_2, c_3); we adopted the following values for them: c_1 = 0.21, c_2 = 0.49, and c_3 = 0.29.[57c] Throughout the calculations, the resolution of the identity approximation[74] has been used with the def2-TZVP/J basis set.[72b,73] Finally, the ZORA has been adopted to treat SR effects. Numerical integrations have been carried out on a dense Lebedev grid (302 points).[75] Simulated spectra of **I**, **II** and **III** have been shifted by 3.2, 10.0 and 10.3 eV, respectively, to superimpose the highest intensity feature of the experimental and simulated L_3-edge, which does not suffer from the extra broadening and the distortion due to the Coster-Kronig Auger decay process.[57j,76] Incidentally, this is needed because absolute theoretical *EE*s carry errors arising from DF deficiencies in the core region, one-particle basis set restrictions and inadequacies in the modelling of spin-free relativistic effects.[57b] A Gaussian broadening factor of 1.0, 1.8 and 1.2 eV has been applied to model $L_{2,3}$-edge NEXAFS spectra of **I**, **II** and **III**, respectively.

2.4 O K-edge and Cr $L_{2,3}$-edges spectra details. Synchrotron radiation NEXAFS measurements were performed at the CNR-IOM beamline ALOISA (Elettra Synchrotron, Trieste).[77] Molecular films were deposited on gold-coated thin glass wafers by thermal evaporation from a homemade crucible of boron nitride in an ultra-high-vacuum environment (base pressure of 10^{-10} mbar during measurements). Title complexes have been evaporated at about the same temperature of ~ 350 K, eventually reaching a max pressure of $3 - 5 \times 10^{-8}$ mbar during evaporation. Along the deposition, we kept the substrate at T_S ~ 220 K, in order to reduce the surface mobility for enhancing dendritic 2D growth, while preventing the sticking of water molecules from the residual gas (whose condensation on Au takes place below 200 K). Finally, we obtained films of ~2.2, ~3.2 and > 6 nm for **III**, **I** and **II** respectively, as estimated from the attenuation of the substrate Au 4f photoemission signal. NEXAFS spectra have been measured keeping the sample at a grazing angle of 6°, while orienting the surface to the magic angle for the incoming linearly polarized X-ray beam. NEXAFS measurements have been performed in partial electron yield by means of a full aperture channeltron placed along the surface normal. The employed channeltron is additionally equipped with a repeller grid in front of it, which is negatively biased to reject secondary electrons and let in the Auger electrons corresponding to the relevant electronic transitions. In particular, we polarized the grid at the voltage of -490 and -550 V for the O 1s and Cr 2p ionization thresholds, respectively. Absolute calibration of the photon energy was obtained for the O 1s and Cr 2p thresholds by simultaneously recording of the drain current on the last mirror of the beamline after the exit slits. The last mirror presents a gold film on top of a Cr and Fe coating, which absorption lines are measurable and used as a reference for the metallic L_3 main peak: Cr at 574.1 eV.[77] Absolute calibration of the O 1s ionization threshold was also obtained by the K-edge absorption line in the drain current due to oxygen contamination (mostly CO) on the surface of the last mirror. This absorption feature was previously calibrated by simultaneously measuring the vibrational structure of the O K-edge threshold from CO gas (central peak at 534.21 eV) thanks to a windowless, differentially pumped, in-line gas ionization cell.[78]

2.5 I, **II** and **III synthesis details.** Title compounds have been prepared as previously reported[79] and purified by means of three recrystallization steps. Compounds purity was confirmed by elemental analysis (EA). IEA, $C_{15}H_{21}CrO_6$: calculated C 51.57 %, H 6.06 %; found: C 51.62%, H 6.08%. IIEA, $C_{15}H_{21}MnO_6$: calculated C 51.14%, H 6.01%; found: C 51.13%, H 5.98%. IIIEA, $C_{15}H_{21}FeO_6$: calculated C 51.01%, H 5.99%; found: C 51.03%, H 6.00%.2.

3. Results and discussion

3.1 Occupied Electronic Structure. The forthcoming discussion may take advantage of a preliminary qualitative description of title molecules' frontier orbitals[80] simply based on symmetry

arguments and overlap considerations. Frontier MOs of a single C_{2v} acac fragment may be split in two sets according to their σ or π character.[81] The former set consists of two completely occupied fragment MOs (FMOs): the in-phase (n_+) and the out-of-phase (n_-) linear combinations of the O lone-pairs, both of them lying in the acac plane. As far as the latter set is concerned, it consists of five FMOs (π_1, π_2 and π_3 DOMOs and π_4 and π_5 VMOs),[31] all of them perpendicular to the acac plane. Moreover, π_j FMOs are symmetric or anti-symmetric with respect to the reflection plane perpendicular to the molecular one and passing through the methinic carbon atom (C(H)) if j is odd (π_o) or even (π_e) (see Fig. 4 of ref. 81), respectively. Finally, as far as the bonding nature of π_4 and π_5 VMOs is concerned, they are both C–O antibonding and mainly localized on the C atoms; additionally, the π_4 VMO has a node on the C(H) atom, while the π_5 one is also C–C(H) antibonding. When three acac fragments are coordinated about TM to generate a regular D_3 TM(acac)$_3$ complex (see Fig. 1),[5] linear combinations of n_+ and π_e FMOs will transform as the D_3 a_1 + e IRs, while those generated by n_- and π_o FMOs will transform as the D_3 a_2 + e IRs. Incidentally, literature data pertaining to the free acac fragment indicate that topmost occupied FMOs (n_+, n_- and π_3) have the following energy ordering: $E_{\pi_3} > E_{n_-} > E_{n_+}$.[81]

As far as the central TM^{III} ion is concerned, its *octahedral* environment lifts the five-fold orbital degeneracy of the TM 3d atomic orbitals (AOs) generating three t_{2g}-like orbitals (a_1 + e in the actual D_3 symmetry of **I** and **III**, and hereafter labelled as $^at_{2g}$ and $^et_{2g}$, respectively)[5,82] and two e_g-like MOs (e in the actual D_3 symmetry of **I** and **III**).[5,82] Accordingly, the HS TM^{III} electronic configuration will be $a^1e^2e^0$(GS = $^4A_2$) in **I**, $a^1e^2e^1$ (GS = ^5E) in **II** and $a^1e^2e^2$ ($^6A_1$) in **III**.[83] The O_h → D_3 descending symmetry allows then us to foresee: i) an extensive mixing among linear combinations of $n_{+/-}$ and $\pi_{e/o}$ acac-based FMOs of e symmetry; ii) the interaction of these linear combinations with both $^et_{2g}$ and e_g-like TM^{III} 3d based orbitals;[82] iii) the unfeasibility of a net distinction between σ and π contributions to the TM–L bonding. Moreover, the relative energy position of frontier acac-based FMOs[81] lets us to predict that the TM–L bonding should be dominated by the interaction between the e TM 3d AOs and the linear combinations of the acac-based $n_{+/-}$ and π_3 FMOs of the same symmetry.[82] Finally, the HS nature of **I**, **II**, and **III** further allows us to expect that: i) the overall interaction between the spin ↑ components of the $n_{+/-}$ and π_3 FMOs and the TM t_{2g}-like 3d AOs will be weakly antibonding in nature for the whole series; ii) the overall interaction between the spin ↑ components of $n_{+/-}$ and π_3 FMOs and the TM e_g-like 3d AOs will gradually weaken the TM–O bonding upon moving from **I** to **III**.

Such a qualitative picture perfectly matches ADF GS results as demonstrated by the inspection of Figs. 2 and 3 where the TM 3d PDOS and the spin ↑ COOPs between TM^{III} 3d AOs and $n_{+/-}$ and π_3 FMOs are displayed, respectively.

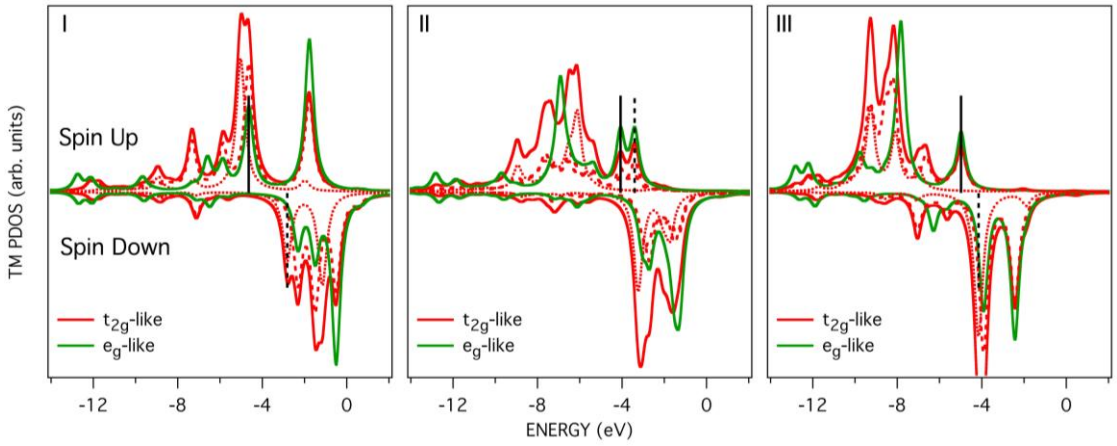

Fig. 2 TM 3d PDOS of the valence states of **I**, **II**, and **III**. Vertical bars correspond to the HOMO (solid lines) and LUMO (dashed lines) energies. Contribution from $^at_{2g}$ (z^2, dotted curves) and $^et_{2g}$ (xy and $x^2 - y^2$, dashed curves) PDOS are also displayed.

The first thing to be noted is the different nature and/or localization of the HOMO and LUMO in the three complexes. According to Liu and Conradie,[29b] the topmost occupied MOs of **I** (the closely spaced 30e(↑) ^{l}HOMO and the 18a_1(↑) ^{l}HOMO-1, see Fig. 2)[84] correspond to the Cr^{III} $^et_{2g}$(↑) and $^at_{2g}$(↑) orbitals strongly mixed with the Cr^{III} e_g-like ones. As suggested on a qualitative ground, the 18a_1(↑) MO is almost completely localized on the Cr 3d z^2 AO (78%), while the $^et_{2g}$ and the e_g-like sets similarly contribute (40% and 27%, respectively) to the ^{l}HOMO, which accounts for a Cr–O antibonding interaction between $^et_{2g}$/e_g-like Cr^{III} AOs and the e combinations of the acac-based π_3 FMO (see Figs. 3 and 4). As a whole, the Cr–O bonding picture emerging from the BP86 results is consistent with a quite extensive mixing between the Cr^{III} 3d AOs and the $(acac)_3^{3-}$-based FMOs; nevertheless, the inspection of Fig. 3 ultimately testifies that the TM–L bonding is dominated by the interaction between the e linear combination of the $(acac)_3^{3-}$-based n_- FMOs and the empty Cr^{III} e_g-like 3d AOs.[85] Useful insights into this matter can be further obtained by referring to Fig. S2 of the ESI† where spin ↑ and spin ↓ COOPs between the TM^{III} e_g-like 3d AOs and the e linear combination of the $(acac)_3^{3-}$-based n_- and n_+ FMOs are displayed. COOP curves make well evident that, according to Pritchard and Autschbach,[86] both the spin ↑ and the spin ↓ component of

the $(acac)_3^{3-}$-based n_- FMOs concur to the dative L → Cr^{III} bonding, while the n_+ contribution is negligible for both spins. Data reported in Figs. 2, 3 and S2 of the ESI† allow the identification of the orbital (the 28e DOMO)[87] accounting for the most relevant contribution to the Cr–O bonding (the participation of the Cr^{III} e_g-like AOs[82] to the 28e(↑) orbital amounts to 8%). As a whole, the Cr–O COOPs reported in Figs. 3 and S2 of the ESI† combined to the Cr–O Nalewajski–Mrozek[88] bond multiplicity index ($^{I}I^{NM}$ = 0.47)[89] and the comparison of Cr/O Hirshfeld(Q_{Hir})[90]/Voronoi(Q_{Vor})[91] gross atomic charges (see Table S1 of the ESI†) with those consistently computed for the isostructural $Al(acac)_3$[92] complex concur to stress the leading role played by the ionic contribution in the Cr–O bonding.

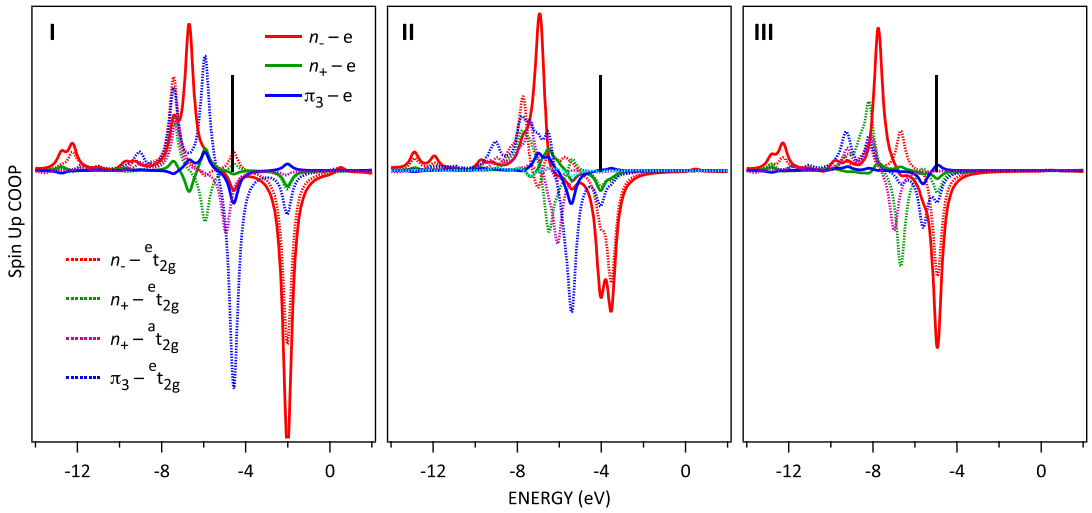

Fig. 3 Spin ↑ COOPs between TM^{III} t_{2g}-like (dotted lines)/e_g-like (solid lines) 3d AOs and $(acac)_3^{3-}$ FMOs in **I**, **II** and **III**. Bonding (antibonding) combinations correspond to positive (negative) peaks in the COOP plot. Vertical bars represent the HOMO energy.

As far as the 18a$_1$(↓) ^{I}LUMO is concerned (see Figs. 2 and 4), it is of some relevance to underline that, differently from the $^{a}t_{2g}$ 18a$_1$(↑) ^{I}HOMO-1, the L participation (64%) involves the a$_1$ combination of the acac-based π_4 FMO (see Fig. 4). As expected, a last look at the left panel of Fig. 2 confirms the presence, among low lying VMOs and rather close to the ^{I}LUMO (ΔE ~ 1 eV), of the Cr^{III}-based e_g-like[82] orbitals (the 32e(↑) VMOs) strongly mixed, as expected, with the $^{e}t_{2g}$ ones.

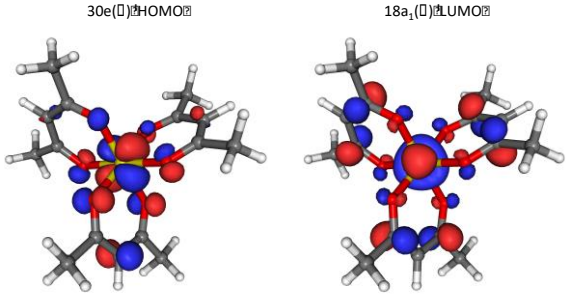

Fig. 4 3D plots of one component of the 30e(↑) ^{I}HOMO and of the 18a$_1$(↓) ^{I}LUMO. Displayed isosurfaces correspond to ±0.05 $e^{1/2}Å^{-3/2}$ values.

It is well known that information about the details of the occupied frontier MOs of volatile compounds may be gained by exploiting the vapour-phase UV PE spectroscopy.[93] He(I) PE spectra of title compounds have been firstly recorded early in the '70s by Evans *et al.*[28a] and, even though Van Dam and Oskam,[28b] the Vovna research group[28c,28f] and Westmore *et al.*[28e] tackled the same problem in the following years, a definitive assignment of title molecules' He(I) lowest lying PE spectral features (*vide infra*), is not yet assessed. In this regard and before anything else, it has to be underlined that: i) He(I) ^{I}PE spectra reported by Akopyan *et al.*,[28c] Westmore *et al.*,[28e] and by Vovna *et al.*[28f] are all consistent with the He(I) ^{I}PE spectrum firstly recorded by Evans *et al.*;[28a,94,95] ii) the whole He(I) ^{II}PE spectral pattern is only present in ref. 28f, but its resolution is very poor; iii) the He(I) ^{III}PE spectrum recorded by Evans *et al.*[28a] is very similar to that collected by Westmore *et al.*[28e] but significantly different from those published for the same molecule by Akopyan *et al.*[28c] and by Vovna *et al.*[28f] In particular, neither the British[28a] nor the Canadian[28e] research group revealed any PE feature between 9.22 and 10.16 eV; at variance to that, the He(I) spectra published by the Vovna group[28c,28f] are both characterized by the presence of a peak that Akopyan *et al.*[28c] placed at 9.64 eV. Finally, similarly to **II**, an extremely weak ^{III}PE feature seems to characterize the lowest IE region of the ^{III}He(I) PE spectrum recorded by Vovna *et al.*[28f]

Van Dam and Oskam[28b] assigned "without any doubt" the lowest lying peak Y (7.46 eV, see Table S2 of the ESI†) of the He(I) ^{I}PE spectrum to the ionization from "metal d-orbitals" by exploiting their relative intensity variations upon switching from the He(I) to the He(II) ionizing source (see Fig. 2 of ref. 28b).[97] Actually, in the habit of the Gelius model,[98] the photoionization cross-section σ_i of the i^{th} MO is

$$\sigma_i = \sum_{n,n\ell} c^{i}_{n\ell,n} S^{n}_{n\ell} \qquad (1)$$

where $(n\ell)$ sums over the states localized on the atomic centres ν and contributing to the ith MO, $S^{n}_{n\ell}$ corresponds to

the atomic subshell photoionization cross-section (ASPCS), and the $c^{i}_{|?|n\ell,n}$ coefficients account for the MO occupancy. According to Berndtsson *et al.*,[99] the $c^{i}_{|?|n\ell,n}$ coefficients are often approximated with the net atomic populations; obviously, this implies to neglect the overlap population contributions to the photoionization cross-section. Now, even though $S^{C}_{|?|2p}$, $S^{O}_{|?|2p}$, and $S^{Cr}_{|?|3d}$ ASPCS decrease upon the He(I) → He(II) switching,[100-101] such a decrease is more pronounced for the $2p^{C/O}$ AOs than for the $3d^{Cr}$ ones. We then expect that the $h\nu^{He(I)} \rightarrow h\nu^{He(II)}$ changing will be associated to a detectable weakening of the ᴵPE features generated by the ionization from L-based MOs.

Spin-unrestricted NR Slater Transition State[102] (ˢTS) calculations for the spin ↑ $18a_1$ and 30e SOMOs have been carried out to approximately take care of the electronic structure relaxation upon ionization. ˢTS outcomes ultimately confirm the assignment of the ᴵPE Y feature to the ionization from "metal d-orbitals" as proposed by Van Dam and Oskam[28b,103] on the basis of their He(II) measurements. More specifically, the weak and broad Y peak at ~ 7.5 eV appears to be generated by the ionization from the 30e(↑) $^{e}t_{2g}$ SOMOs ($^{S}TS_{30e(\uparrow)}$ = 6.84 eV, see Table 2 of the ESI†), strongly mixed with the e_g-like ones (see Fig. 2), while ˢTS results pertaining to the $^{a}t_{2g}$ $18a_1$(↑) SOMO ($^{S}TS_{18a1(\uparrow)}$ = 7.47 eV) suggest that its ionization should be hidden under the lower IE side of the following PE feature (the band A centred at 8.06 eV in the He(I) ᴵPE spectrum recorded by Evans *et al.*[28a]) together the ionization from the π_3 acac-based $15a_2$ DOMO whose IE appears to be substantially TM independent[105] (8.06,[28a] 8.14,[28a] 8.10,[28a] and 8.18[28d] eV in **I**, **II**, **III**, and $Al(acac)_3$, respectively) as a consequence of the absence of any 3d AO transforming as the a_2 IR in the D_3 symmetry point group.

The electronic structure of **II**, when compared to **I**, is characterized by the presence of an extra electron. According to our preliminary qualitative considerations, such an electron will i) asymmetrically occupy the Mn 3d-based e_g-like orbitals; ii) induce the genuine Jahn-Teller[47] distortion (see the Computational and Experimental Details) characterizing the γ structure of **II**;[19c] iii) lift the degeneracy of the Mn^{III} 3d-based e_g-like levels. Similarly to **I**, ᴵᴵGS ADF results confirm our prediction indicating the 94a(↑) ᴵᴵHOMO and the 95a(↑) ᴵᴵLUMO (see the central panel of Fig. 2) as the Mn^{III} e_g-like orbitals (strongly mixed with the $^{e}t_{2g}$ ones), which account for the σ Mn–O antibonding interaction with the e linear combination of the acac-based *n*- FMO (see Figs. 3, 5 and S2 of the ESI†). Incidentally, the bonding partners of the 94a(↑) ᴵᴵHOMO and the 95a(↑) ᴵᴵLUMO correspond to the 85a and 86a DOMOs whose spin ↑ components lie at -6.98 and -6.88 eV, respectively (see Figs. 2 and 3). Despite the absence of any symmetry element, it is then possible not only to recognize t_{2g}- and e_g-like orbitals among the frontier MOs of **II** but also to assess that the former set appears much more atom-like in **II** than in **I**, while the e_g-like contribution to the TM–L interaction is rather similar in the Cr^{III} and Mn^{III} complexes (see Figs. 2, 3 and S2 of the ESI†).[106]

Useful information about this matter may be gained by exploiting the Ziegler transition state (^{Z}TS)[50] scheme.[107] As a matter of fact, ᴵᴵBE is computed less negative than ᴵBE by 27 kcal/mol (see Table S1 of the ESI†), and two contributions oppositely participate to this finding: the ΔE_{ster} term, lower in **II** than in **I** as a consequence of the Jahn-Teller distortion,[19c,47] and the ΔE_{int} term, much less negative in **II** than in **I** (the absence of any symmetry element in **II** prevents any ᴵᴵΔE_{int} partitioning into contributions from distinct IRs). Besides the effects associated to the minor differences characterizing the structural arrangement of the $(acac)_3^{3-}$ fragment around the TM^{III} ions (see Fig. S3 of the ESI†), the $|^{II}\Delta E_{int}| < |^{I}\Delta E_{int}|$ result is directly related to the weakening of the TM–O interaction induced by the presence of the extra electron occupying the e_g-like 94a(↑) ᴵᴵHOMO,[106] whose antibonding character with respect to the σ Mn–O interaction has been already stressed. Taking **I** as a reference once again, it is interesting to note that $^{II}I^{NM} \sim {}^{I}I^{NM}$ when considering the $(Mn–O)^{s}$ bonds, while $^{II}I^{NM} \sim ½\ {}^{I}I^{NM}$ for the $(Mn–O)^{I}$ ones (see Table S1 of the ESI†). Such a result may be straightforwardly rationalized by looking at the 94a(↑) ᴵᴵHOMO and the 95a(↑) ᴵᴵLUMO 3D plots (see Fig. 5). Similarly to **I**, "only" the Mn 3d-based t_{2g}-like orbitals are involved in the four $(Mn–O)^{s}$ bonds; while an e_g-like antibonding SOMO is also involved when the two $(Mn–O)^{I}$ ones are considered.

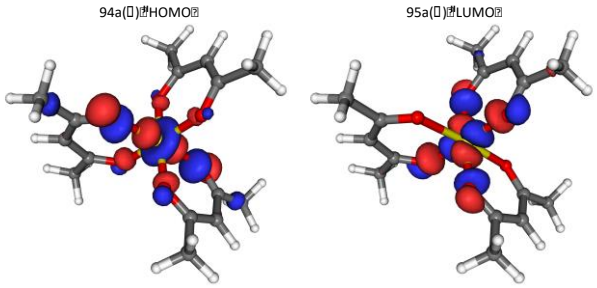

Fig. 5 3D plots of the 94a(↑) ᴵᴵHOMO and 95a(↑) ᴵᴵLUMO. Displayed isosurfaces correspond to ±0.05 $e^{1/2}Å^{-3/2}$ values.

Before moving to the analysis of the He(I) ᴵᴵPE features,[28a,28f,94,95] it is worth of note that theoretical outcomes so far considered are perfectly in tune with structural data reported in Table S3 of the ESI†, where selected optimized geometrical parameters for title complexes are compared with corresponding X-ray crystallographic results[8c,19b] and the DFT–B3LYP structures reported by Diaz-Acosta *et al.*[8c-8d] (optimized coordinates of **I**, **II** and **III** are reported in Tables S4, S5 and S6 of the ESI†, respectively). In more detail, the inspection of Table S3 of the ESI†, reveals that BP86 structural parameters quantitatively agree with both the X-ray crystallographic results[8c,19b] and DFT–B3LYP literature data.[8c-8d] Incidentally, as already mentioned, the ligand geometrical parameters appear to be negligibly affected along the series (see Fig. S3 of the ESI†).

Similarly to **I**, the spin-unrestricted NR ˢTS calculations[102] carried out for the topmost spin ↑ MOs prompt us to assign with confidence the very weak He(I) Y feature of the ᴵᴵPE to the ionization from the 94a(↑) ᴵᴵHOMO ($^{S}TS_{94a(\uparrow)}$ = 6.34 eV), i.e., the

Mn 3d-based e_g-like SOMO antibonding in character with respect to the Mn–O σ interaction (see Fig. 5). As far as the broad band A and the evident shoulder on its lower IE side are concerned (see Fig. 1 of ref. 28f), they are together associated to the ionization from the three linear combinations of the π_3 acac-based FMOs (the 93a – 91a DOMOs). Two reasons concur to minimize the splitting between the e and the a_2 linear combinations of the π_3 acac-based FMOs revealed in **I**: i) the absence of any symmetry elements in **II** allows a similar participation of Mn 3d-based AOs (~11%) to the π_3-based spin ↑ MOs; ii) the Mn t_{2g}-like SOMOs are more atom-like in **II** than in **I** (see Fig. 2), so that their interaction with π_3-based spin ↑ MOs is poorer in **II** than in **I** (see Fig. 3).

The symmetric occupation of the 31e ᴵᴵᴵHOMO prevents any Jahn-Teller[47] distortions of the ᴵᴵᴵGS structure and, despite the absence of any doubt about the 31e ᴵᴵᴵHOMO nature (strongly antibonding in character with respect to the Fe–O σ interaction, see Figs. 3, 6 and S2 of the ESI†), it deserves to be underlined that the overall participation of the Fe 3d AOs to the 31e ᴵᴵᴵHOMO amounts to 33% with a comparable contribution of $^{e}t_{2g}$ (19%) and e_g-like (14%) levels. It is then at least hasty to label the ᴵᴵᴵHOMO as Fe 3d-based SOMOs.[29a]

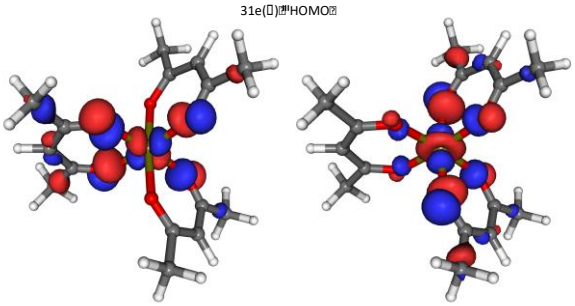

Fig. 6 3D plots of the 31e(↑) ᴵᴵᴵHOMO. Displayed isosurfaces correspond to ±0.05 $e^{1/2}Å^{-3/2}$ values.

Even more unlikely appears the assessment of a SOMO nature[29a] for the 30e MO, whose localization on the Fe 3d-based AOs appears negligible (see Fig. 6 of ref. 29a). As such, the antibonding nature of the Fe e_g-like spin ↑ MOs (see Figs. 3, 6 and S2 of the ESI†) and the "non-bonding" character of the Fe t_{2g}-like ones (see Fig. 3), make hard to justify not only the close spacing between $^{e}t_{2g}$ and e_g-like SOMOs but also the rather large ΔE (~ 2 eV) between $^{e}t_{2g}$ and $^{a}t_{2g}$ SOMOs (see Fig. 6 of ref. 29a).

Similarly to **I** and **II**, the BP86 optimized structural parameters of **III** agree very well with both the X-ray crystallographic results and the DFT–B3LYP structures reported by Diaz-Acosta *et al.*[8c] (see Table S3 of the ESI†). Interestingly, the Fe–O bond distances are intermediate between the Cr–O and the (Mn–O)ᴵ ones. Such a result, perfectly mirrored by the corresponding ᴵᴵᴵI^{NM} value, is the consequence of the presence of two electrons in the two e_g-like(↑) SOMOs (the bonding partners correspond once again to the 28e(↑) MOs, whose localization on the Fe^{III} e_g-like AOs amounts to 48%, see Figs. 2 and 3). Incidentally, the larger I^{NM} decrease upon moving from **I** to **II** than from **I** to **III** is simply due to the different localization of the 94a(↑) (in **II**) and 31e(↑) (in **III**) SOMOs (compare the corresponding 3D plots in Figs. 5 and 6, respectively). According to that, ᴵᴵᴵBE is evaluated less negative than ᴵBE by 61 kcal/mol (see Table S1 of the ESI†), and the major role in determining such an evidence is the reduced e contribution (~100 kcal/mol) to ΔE_{int} as a consequence of the antibonding character of the symmetrically occupied 31e(↑) ᴵᴵᴵHOMO.

Before considering the lowest lying He(I) ᴵᴵᴵPE spectrum assignment, two further remarks have to be done: i) as qualitatively anticipated by Pritchard and Autschbach,[86] only the spin ↓ component of the $(acac)_3^{3-}$-based *n.* FMOs concur to the dative L → Fe^{III} bonding (see Fig. S2 of the ESI†); ii) even though the Fe–O interaction is certainly the most covalent among the investigated molecules (see the Ω^{Fe}_{Hir} and Ω^{Fe}_{Vor} values in Table S1 of the ESI†, and consider the 48% participation of the Fe^{III} e_g-like AOs to the 28e(↑) MOs), the overall effect of such an increased symmetry-restricted covalency[42] is the Fe–O bond weakening.

Besides the already mentioned differences between the He(I) ᴵᴵᴵPE spectra recorded by the British[28a]/Canadian[28e] research groups and that of Vovna[28c,28f] in the IE region ranging from 9.22 to 10.16 eV, it has to be also underlined that the He(I) ᴵᴵᴵPE spectrum recorded by the Russian group (see Fig. 1 of ref. 28f), similarly to **II**, seems to be characterized by the presence of an almost imperceptible feature at low IEs. In this context, it is of some relevance to remind the literature debate between the Lloyd and Orchard groups about the "weak low-ionisation-energy band in the He(I) photoelectron spectrum of $Fe(hfa)_3$", which took place early in the seventies.[108,109] Spin unrestricted NR ^{S}TS calculations[102] carried out for the symmetrically occupied 31e(↑) ᴵᴵᴵHOMO provide a theoretical estimate of the lowest IE ($^{S}TS_{31e(↑)}$ = 6.95 eV) which would prompt us to agree with the Lloyd's assignment,[96] even though the presence of a shadow of the prominent PE band A[109] cannot be ruled out.

3.2 Unoccupied Electronic Structure. Dipole allowed transitions imply that[52]

$$\Gamma_{GS} \otimes \Gamma_{\mu} \otimes \Gamma_{ES} \supset \Gamma_{Sym} \qquad (2)$$

where Γ_{GS}, Γ_{μ}, Γ_{ES} and Γ_{Sym} correspond to the IRs of the TM(acac)$_3$ electronic GS (a_2 in **I**, e in **II**, and a_1 in **III**),[46] the dipole moment operator (a_2 + e),[52] the electronic ES ($\Gamma_{iso} \otimes \Gamma_{GS} \otimes \Gamma_{fso}$),[52] and the totally symmetric representation (a_1) of the idealized TM(acac)$_3$ point group (D_3), respectively. Eqn (2) may then evolve to

$$\Gamma_{GS} \otimes a_2 \otimes \Gamma_{iso} \otimes \Gamma_{GS} \otimes \Gamma_{fso} = a_2 \otimes \Gamma_{iso} \otimes \Gamma_{fso} \supset a_1 \qquad (3a)$$

$$\Gamma_{GS} \otimes e \otimes \Gamma_{iso} \otimes \Gamma_{GS} \otimes \Gamma_{fso} = e \otimes \Gamma_{iso} \otimes \Gamma_{fso} \supset a_1 \qquad (3b)$$

pointing out that, within the approximation, which reduces the complete one-electron excited configuration space (1h–1p space) to the subspace where only the core electrons are excited, the allowed electric dipole transitions imply

$$G_{iso} \ddot{A} G_{fso} = a_2 \quad (4a)$$

$$G_{iso} \ddot{A} G_{fso} = e \quad (4b)$$

In the D_3 point group, electric dipole transitions forbidden by symmetry are then limited to the $a_1 \rightarrow a_1$ and $a_2 \rightarrow a_2$ ones.[52]

Wang and Ziegler[110] have shown that spin-unrestricted TD-DFT calculations are able to provide a rather accurate evaluation of *EE*s even when dealing with open shell molecules.[36b] Lowest lying electronic excitations from the $1s^O$-based DOMOs (the $3a_1 + 2a_2 + 2e + 3e$ TM(acac)$_3$ orbitals, TM = Cr and Fe)[111] will involve transitions to: i) TM based $^at_{2g}$ and $^et_{2g}$ SOMOs;[7] ii) TM based e_g-like VMOs/SOMOs;[7] iii) linear combinations of the acac-based π_4 VMO. Along the whole **I** – **III** series, transitions from the $1s^O$-based DOMOs to the $^at_{2g}$ and $^et_{2g}$ SOMOs[7] cannot affect the GS spin multiplicities. In fact, ESs associated to the $t_{2g}^4e_g^0$ (**I**), $t_{2g}^4e_g^1$ (**II**), and $t_{2g}^4e_g^2$ (**III**) excited electronic configurations will necessarily correspond to quartets in **I**, quintets in **II** and sextets in **III**, if spin contamination is neglected. The same holds for transitions from the $1s^O$-based DOMOs to the e_g-like SOMOs[7] in **III**. The situation is much more complicated when VMOs are involved; i.e., Cr^{III}/Mn^{III} 3d-based e_g-like orbitals or linear combinations of the acac-based $\pi_{e/o}$ virtual FMOs. For instance, in **I** the $3a_1^2 \rightleftharpoons 32e^0 \rightarrow 3a_1^1 \ldots 32e^1$ electronic excitation (the 32e MO corresponds to the Cr^{III} e_g-like VMOs) may generate one sextet state (^{6}E), two quartet states (^{4}E), and a doublet state (^{2}E). Quartet → sextet and quartet → doublet excitations, implying spin–flip or double excitation processes, will be ignored herein and, similarly to our studies on the CuPc,[63e] CuTPP[63g] and CuTPP(F)[63g] ^{N}K-edges, the ^{O}K-edge spectra of title compounds will be assigned by limiting our attention to excitations involving the same GS spin multiplicity.[7]

Upon 2p → 3d one-electron excitation, the TM^{III} final electronic configuration is $2p^53d^4$ in **I**, $2p^53d^5$ in **II** and $2p^53d^6$ in **III**. If the whole set of multiplets arising from the $3d^{4/6}$ ($3d^5$) configurations is collectively labelled as $D^{4/6}$ (D^5),[112] the electronic states generated by the $2p^53d^{4/6}$ ($2p^53d^5$) configuration are: $^2P \otimes D^4 = {}^{2,4}S, {}^{2,4,6}P, {}^{2,4,6}D, {}^{2,4,6}F, {}^{2,4}G, {}^{2,4}H, {}^{2,4}I, {}^2K$ ($^2P \otimes D^5 = {}^{1,3,5}S, {}^{1,3,5,7}P, {}^{1,3,5}D, {}^{1,3,5}F, {}^{1,3,5}G, {}^{1,3,5}H, {}^{1,3}I, {}^{1,3}K$).[112] As a consequence of the ligand-field, covalent interactions and SOC admixture, these states will further split to generate a total of 6 × 210 = 1260 (6 × 252 = 1512) molecular magnetic spin sublevels with $M_S = \pm1/2, \pm3/2, \pm5/2$ ($M_S = 0, \pm1, \pm2, \pm3$). Reference to the TM^{III} electronic configuration in **I**, **II**, and **III**[7] allows us to foresee that the one-electron excitation pattern describing Cr^{III} and Mn^{III} final states in the D_3 structure will include states having spin multiplicity either equal to ($\Delta S = 0$) or lower/higher than ($\Delta S = \pm1$) the GS one ($^ IS = 3/2$; $^{II}S = 2$), a consequence of the presence of empty 3d-based MOs in both cases.[117] At variance to that, the one-electron excitation pattern describing the Fe^{III} final states will be dominated by states having a spin multiplicity equal to ($\Delta S = 0$) or lower than ($\Delta S = -1$) the GS one ($^{III}S = 5/2$).[117] We showed elsewhere[35] that these excitations involve mainly DOMO → SOMO transitions.

3.2.1 O K-edge spectra. The pre-edge *EE* region of the ^{O}K-edge spectra of title molecules is displayed in Fig. 7 for the D_3 **I** and **III** and in Fig. 8 for the C_1 **II**.

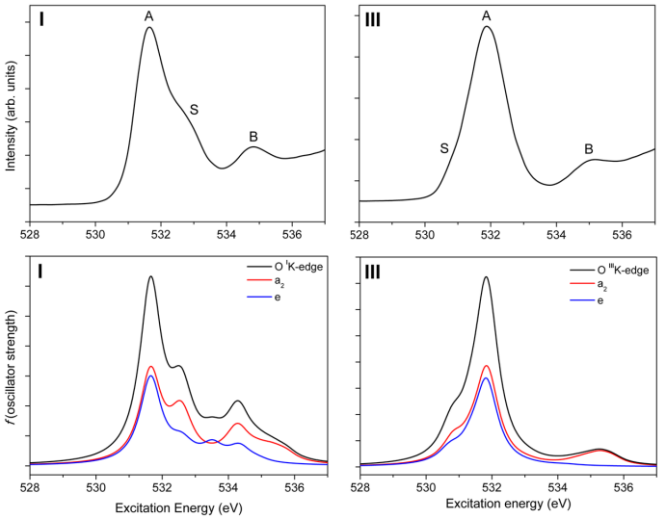

Fig. 7 Experimental (upper panels) and simulated (lower panels) ^{O}K-edge spectra of **I** (left panels) and **III** (right panels). Contributions from a_2 and e symmetries in the SR ZORA TD-DFT $1s^O$ excitation spectra of **I** and **III** are also displayed. $1s^O$ SR-ZORA ionization limits evaluated by adopting the LB94 functional[68] are 534.9 eV (**I**) and 534.6 eV(**III**). Both simulated spectra have been shifted by 12.2 eV and have a Gaussian broadening of 0.4 eV.

It is well known that the electric dipole allowed[52] $1s^L \rightarrow mp^L$ transitions intensity quantifies the participation of the L donor atom *m*p AOs to the unoccupied frontier MOs.[59-61] Unfortunately, data herein reported do not allow to achieve a reliable quantitative comparison of the experimental intensities because of the significantly different thickness of the molecular films, which likely yielded different morphologies.

Along the whole **I** – **III** series, the ^{O}K pre-edge *EE* region appears as an asymmetric broad and intense band centred at ~ 531.5 eV followed by a much less intense feature at ~ 535 eV. The main peak (A, in Figs. 7 and 8) has a rather similar shape in **I** and **II**, while the details of the spectral pattern of **III** appear quite different with respect to those of **I** and **II** (compare the upper panels of Fig. 7 and the spectrum reported in Fig. 8). In fact, both in **I** and **II** a shoulder S (much more evident in **I**) is present on the higher *EE* side of A, while an equally evident shoulder is present only on the lower *EE* side of A in **III**. All together, it is patent that the experimental information provided by ^{O}K-edge spectra is not particularly reach. Thus, only the combined use of symmetry, orbitals and spectra appears to be the Hobson's choice to get some information from the experimental evidences. *EE*s and *f* values associated with the $1s^O$ excitation spectrum as obtained from spin-unrestricted SR-ZORA TD-DFT calculations carried for **I**, **II** and **III** are reported in Tables S7 – S9 of the ESI†, respectively, while the corresponding $^{I/III}f$ distributions in the *EE* range 528 – 537 eV are displayed in Fig. 7 (lower panels), where e + a_2 contributions are also included, and in Fig. 8. The agreement between the $1s^O$ excitation spectrum of **I** and the ^If distribution is amazing. Theoretical results included in Table S7 of the ESI†

allow us to assign with confidence the main feature A of the ^{O}K-edge NEXAFS spectrum of **I** to states generated by the two lowest lying and accidentally degenerate $1s^{O} \rightarrow \pi_4$ transitions. In both cases, the presence of the $18a_1(\downarrow)$ ^{I}LUMO (sizably localized on the Cr^{III} 3d z^2 AO) among the corresponding fsos deserves to be stressed. As far as the shoulder S on the higher *EE* side of A is concerned, major contributions come from states associated to $1s^{O} \rightarrow e_g$-like($\uparrow$) LMCT excitations. According to spin-unrestricted SR-ZORA TD-DFT results, high lying VMOs are involved in states contributing to B.

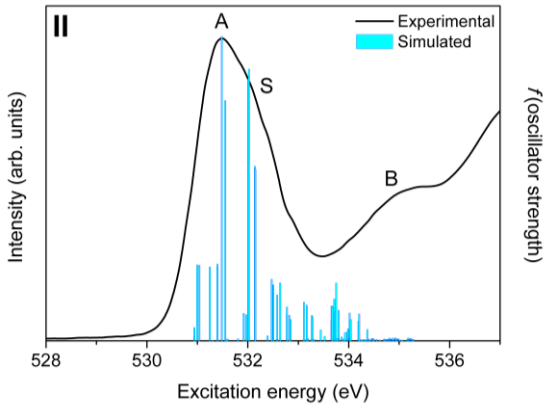

Fig. 8 Experimental and simulated ^{O}K-edge spectra of **II**. The $1s^{O}$ SR-ZORA ionization limit evaluated by adopting the LB94 functional[68] is 534.8 eV (mean value). Theoretical *EE*s have been shifted by 12.6 eV and reported as vertical steaks because the optimized structure of **II** has no symmetry.

Even though the absence of any symmetry elements in the optimized structure of **II** does not allow a straightforward distinction between e and a_2 excitations, the overall agreement between theory and experiment is once again startling (see Fig. 8). Interestingly, the lower *EE* side of the main feature A is generated by states all of them involving $1s^{O} \rightarrow 95a(\uparrow)$ ^{II}LUMO LMCT excitations (see Table S8 of the ESI†). Similarly to **I**, two quasi degenerate excitations contribute to A in the $1s^{O}$ NEXAFS spectrum of **II**. Even though major contributions come in both cases from $1s^{O} \rightarrow \pi_4$ transitions, the inspection of Table S8 of the ESI† reveals a tiny LMCT participation. At least four transitions are present on the higher *EE* side of A (see Table S8 of the ESI†), which, once again, mainly involve $1s^{O} \rightarrow \pi_4$ excitations.

It has been already mentioned that the ^{O}K-edge NEXAFS spectrum of **III** reveals minor, but well evident, differences with respect to the spectral patterns of **I** and **II**. The agreement between theory and experiment (see Fig. 7, right panels) makes us confident about the possibility of shedding light into this matter. *EE*s and *f* values associated with the $1s^{O}$ excitation spectrum as obtained from spin-unrestricted SR-ZORA TD-DFT calculations carried for **III** are reported in Tables S9 of the ESI† while the ^{III}f distribution in the *EE* range 528 – 537 eV is shown in Fig. 7 together the e + a_2 contributions. Data included in Table S9 of the ESI† allow us to assign the shoulder S on the lower *EE* side of the main feature A to states generated by $1s^{O} \rightarrow {}^{a/e}t_{2g}$-like($\downarrow$) LMCT transitions. Several, closely spaced excitations contribute to A (see Table S9 of the ESI†); among them, the ones characterized by the largest ^{III}f values (33.4×10^{-3} and 34.9×10^{-3}) are accidentally degenerate and purely $1s^{O} \rightarrow \pi_4$ in nature.

3.2.2 TM^{III} $L_{2,3}$-edges spectra. The simulated $^{I}L_{2,3}$-edges spectrum is compared in Fig. 9 with the experimental one.

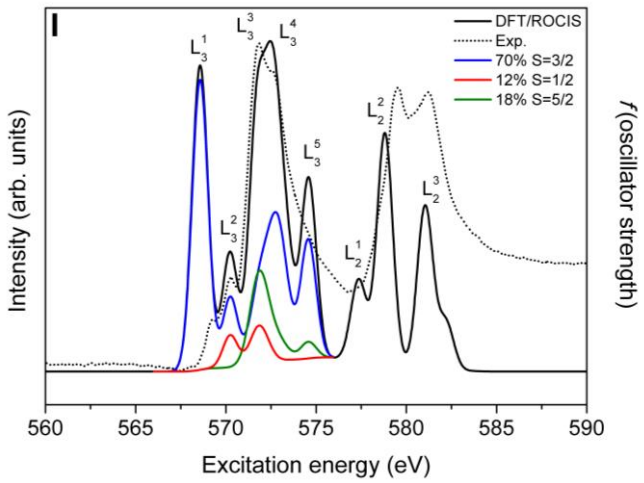

Fig. 9 Simulated (black solid line) and experimental (black dotted line) $L_{2,3}$-edges spectrum of **I**. Blue, green and red lines represent deconvolution of the simulated spectrum in terms of states with different spin multiplicity (S). The simulated spectrum has been shifted by 3.2 eV and has a Gaussian broadening of 1.0 eV.

Despite relative positions and shapes of the L_3 features are correctly reproduced, the opposite is true when the $^{I}L_3{}^{1}$ and $^{I}L_3{}^{2}$ relative intensities are considered. As such, it is noteworthy that in the "L-edge X-ray absorption study of mononuclear vanadium complexes and spectral predictions using a restricted open shell configuration interaction ansatz" Maganas *et al.*[57j] pointed out that the relative intensity of the simulated lowest lying L_3 feature of the $V(acac)_3$ NEXAFS spectrum is dramatically influenced by the adopted functional and the selected semi-empirical parameters c_1, c_2, and c_3 (see the panel C of Fig. 5 in ref. 57j). Here, rather than adopting different functionals and/or different c_1, c_2, and c_3 values for different species to obtain the best agreement between theory and experiment, we preferred to adopt, throughout the paper, the same functional and the same set of c_1, c_2, and c_3 values to favour the comparison between homogeneous theoretical results.

The inspection of Fig. 9 testifies that most relevant contributions to the lower $^{I}L_3$ *EE* region (below 571 eV) arise from states having either GS (S = 3/2, ΔS = 0) or lower (S = 1/2, ΔS = -1) spin multiplicity. Moreover, states associated to the $^{I}L_3{}^{1}$ (S = 3/2, > 95%) and $^{I}L_3{}^{2}$ (S = 3/2, 62%) features lying at *EE* = 568.6 and 570.2 eV, respectively, mainly involve Cr^{III}-based 2p $\rightarrow {}^{a/e}t_{2g}$ single electronic excitations. The successive broad and intense band envelope centred at 572.5 eV consists of two evident features, $^{I}L_3{}^{3}$ and $^{I}L_3{}^{4}$ at *EE* = 571.9 and 572.5 eV, respectively. States with ΔS = 0 and ΔS = ± 1 (28, 34 and 15%, respectively, see Fig. 9) similarly contribute to $^{I}L_3{}^{3}$, while $^{I}L_3{}^{4}$ mainly include (57%) states with ΔS = 0. In more detail, states having the GS spin multiplicity and contributing to $^{I}L_3{}^{3}$ involve Cr^{III}-based single (16%) 2p $\rightarrow {}^{e}t_{2g}$ transitions and

coupled-single[57j] (84%) 2p → $^{a/e}t_{2g}$ SOMOs and $^{a/e}t_{2g}$ SOMOs → e_g-like VMOs excitations. At variance to that, states with S = 5/2 (ΔS = +1) and S = 1/2 (ΔS = -1) mainly involve single 2p → π_4 metal-to-ligand charge transfer (MLCT) transitions. States with ΔS = 0 (57%) and contributing to $^{I}L_3^4$ involve the same, just mentioned, 2p → $^{a/e}t_{2g}$ SOMOs and $^{a/e}t_{2g}$ → e_g-like coupled-single excitations. As far as the highest *EE* peak of the L_3 region is concerned ($^{I}L_3^5$ at *EE* = 574.6 eV in Fig. 9), it mainly (66%) includes states with ΔS = 0, which involve coupled-single electronic excitations. Nevertheless, it has to be underlined that these transitions now correspond to 2p → $^{a/e}t_{2g}$ SOMOs and $^{a/e}t_{2g}$ SOMOs → π_4 VMOs MLCT excitations and differently from $Mn(acac)_2$,[35] $Co(acac)_2$,[35] FePc[119] and FePc(η^2-O_2)[119] do not imply states with ΔS = -1. It is well known that main discrepancies between theory and experiment affect the L_2 region;[57j] nevertheless, it is of some relevance to mention that the DFT/ROCIS $^{I}L_2^2$ – $^{I}L_3^3$ Δ*EE* (7 eV) satisfactorily reproduces the experimental value (7.5 eV). Any further assignment of the $^{I}L_2$ feature is herein avoided as this *EE* region is not unambiguously determined by experiment.[57j]

The $^{II}L_{2,3}$-edges NEXAFS spectrum, firstly recorded by Grush *et al.*,[120] is superimposed to the simulated one in Fig. 10. The overall agreement between theory and experiment is definitely better than that obtained for **I**. In fact, not only the relative energy positions and the shape of the simulated L_3 features nicely match the experimental evidences, but also their relative intensities are properly reproduced by DFT/ROCIS calculations. As a whole, the $^{II}L_3$ spectrum is characterized by the presence of four spectral features. Similarly to **I**, the lowest lying ones ($^{II}L_3^1$ and $^{II}L_3^2$ at *EE* = 639.5 and 640.8 eV, respectively) are dominated (90 and 69%, respectively) by states having the same GS multiplicity and involving Mn^{III}-based 2p → 3d electronic excitations. In more detail, the $^{II}L_3^1$ shoulder involves only 2p → $^{a/e}t_{2g}$ SOMOs transitions, while the most intense $^{II}L_3^2$ peak also involves the 2p → e_g-like SOMO excitation. Incidentally, states with ΔS = -1 and involving 2p → VMO MLCT transition faintly (14%) contribute to $^{II}L_3^2$. Alike $^{II}L_3^1$ and $^{II}L_3^2$, states with ΔS = 0 mainly contribute (51%) to the generation of the $^{II}L_3^3$ feature at 642.7 eV; nevertheless, coupled-single 2p → SOMOs and SOMOs → VMO electronic excitations are predominant (86%). It is worthwhile to mention that, both the SOMOs ($^{a/e}t_{2g}$ and e_g-like) and the VMO (e_g-like), are Mn^{III} 3d-based MOs. As far as the remaining 14% is concerned, it is generated by the 2p → e_g-like SOMO single excitation. Even though tiny, contributions to $^{II}L_3^3$ from states with ΔS = +1/-1 (15%/11%) cannot be ignored and they mainly involve 2p → VMOs MLCT transitions (see Fig. 10). States having the GS spin multiplicity (ΔS = 0) highly contribute (69%) to the highest lying $^{II}L_3^4$ feature at 645.2 eV, and likewise $^{II}L_3^3$ both coupled-single (81%) and single (19%) electronic excitations are involved. Nevertheless, similarly to **I**, VMOs systematically correspond to the linear combinations of the π_4 acac-based FMO. In more detail, both the single electronic excitations (2p → π_4) and the coupled-single 2p → $^{a/e}t_{2g}$ and e_g-like → π_4 transitions have a MLCT character. As a final remark, states with ΔS = ± 1 contribute to the $^{II}L_3^2$ and $^{II}L_3^3$ central peaks (see Fig. 10), represent a 27% of the total transitions and mainly involve high-lying acac-based VMOs. The theoretical Δ*EE* between $^{II}L_2^1$ and $^{II}L_3^2$ (10 eV) semiquantitatively reproduce the experimental value (~11eV),[120-121] but no further assignment of $^{II}L_2$ features is herein attempted as this region is not unambiguously determined by experiment.

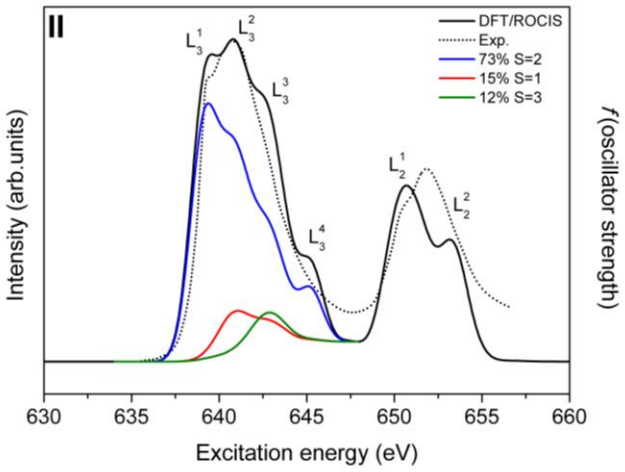

Fig. 10 Experimental (black dotted line) and simulated (black solid line) $L_{2,3}$-edges spectra of **II**. Blue, green and red lines represent deconvolution of the simulated spectrum in terms of states with different spin multiplicity (S). The simulated spectrum has been shifted by 10.0 eV and has a Gaussian broadening 1.8 eV. Experimental spectrum was digitalized from the ref. 120.

The $^{III}L_{2,3}$-edges NEXAFS spectrum[8h] is superimposed to the simulated one in Fig. 11. The overall agreement is very good; positions, shapes and relative intensities of experimental features are properly reproduced both in the in $^{III}L_3$ and $^{III}L_2$ regions.

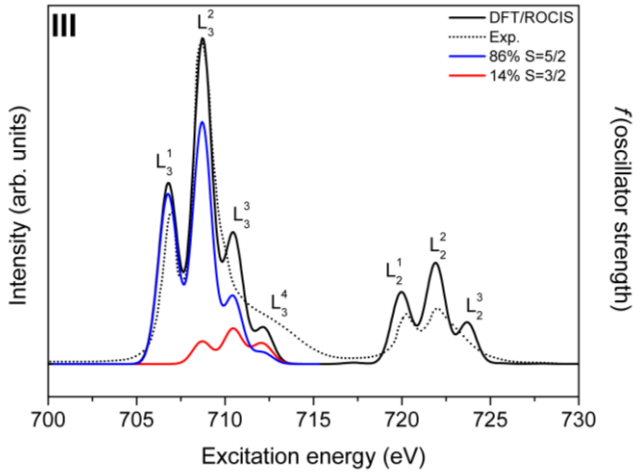

Fig. 11 Experimental (black dotted line) and simulated (black solid line) $L_{2,3}$-edges spectra of **III**. Blue and red lines represent deconvolution of the simulated spectrum in terms of states with different spin multiplicity (S). The simulated spectrum has been shifted by 10.3 eV and has a Gaussian broadening 1.2 eV. Experimental spectrum was digitalized from the ref. 8h.

The well defined, lowest lying $^{III}L_3^1$ peak (*EE* = 708.3 eV) mainly includes (94%) states characterized by ΔS = 0 and generated by 2p → $^{a/e}t_{2g}$ SOMOs single electronic excitations.

Even though both states with $\Delta S = 0$ and $\Delta S = -1$ contribute to the most intense peak $^{III}L_3{}^2$ (*EE* = 710.1 eV), the former (75%) significantly exceed the latter (see Fig. 11) and they are associated to 2p → e_g-like single electronic excitations. As far as states with $\Delta S = -1$ are concerned, they involve MLCT transitions from the whole Fe^{III} 2p set to the e linear combination of the acac-based π_4 FMO.

On the higher energy side of $^{III}L_3{}^2$ there are two well evident shoulders ($^{III}L_3{}^3$ and $^{III}L_3{}^4$ at 711.8 and 713.5 eV, respectively). Both states with $\Delta S = 0$ and $\Delta S = -1$ contribute to the $^{III}L_3{}^3$ (51% *vs* 27%, respectively); moreover, Fe^{III}-based single electronic excitations (2p → e_g-like) are involved in $\Delta S = 0$ states, while MLCT 2p → π_4 transitions contribute to $\Delta S = -1$ states. Very similar considerations can be done for electronic excitations associated to states generating $^{III}L_3{}^4$, the only difference being the higher percentage of states with $\Delta S = -1$ (59%) with respect to those characterizes by the GS spin multiplicity (34%). As already mentioned, DFT/ROCIS calculations quantitatively reproduce the $^{III}L_2 - {}^{III}L_3$ ΔEE (~13 eV, see Fig. 11), but for the same reasons previously underlined we do not attempt any detailed assignment of this *EE* region.

Conclusions

Occupied and empty states of HS $Cr(acac)_3$, $Mn(acac)_3$, and $Fe(acac)_3$ complexes have been thoroughly investigated. Ground states of the three complexes have been comparatively studied by considering the same *octahedral* coordinative environment of the TM^{III} ion, the same oxidation number of the TM^{III} ion, the same number of $^{TM}t_{2g}$-like electrons, and the progressive increasing of the $^{TM}e_g$-like electron number. The TM–L bonding scheme of the D_3 $Cr(acac)_3$ appears to be dominated by ionic interactions, while the D_3 $Fe(acac)_3$ results the most covalent among the investigated complexes. Despite such an evidence, the use of the Ziegler transition state approach allowed us to state that the $Fe(acac)_3$ bonding energy is significantly lower than the $Cr(acac)_3$ one as a consequence of the symmetric occupation of the Fe 3d-based e_g-like orbitals, Fe–O σ antibonding in nature. Occupied frontier orbitals have been also studied by exploiting vapour-phase He(I) and, when available, He(II) literature PE data. Experimental evidences, nowadays not yet definitely assigned, have been discussed and compared with the outcomes of numerical experiments carried out in the framework of the DFT and by exploiting the Slater transition state method. Insights into the title molecules empty states have been gained by combining NEXAFS data at the ^{O}K-edge as well as at the $^{TM}L_{3,2}$-edges with scalar relativistic ZORA TD-DFT and DFT/ROCIS calculations, respectively. Similarly to other TM complexes characterized by the presence of ligands with low lying empty π^* orbitals, the higher *EE* side of the $^{I/II/III}L_3$-edge systematically includes states, which involve metal-to-ligand-charge-transfer transitions. The good agreement between experiment and theory certainly encourages us to apply both approaches to different ligands and corresponding TM complexes when interested to look into K-edge and $L_{3,2}$-edges evidences.

Acknowledgements

The Italian Ministry of the University and Research (PRIN-2010BNZ3F2, project DESCARTES), the Università degli Studi di Padova (CPDA134272/13, project S_3MArTA), the Computational Chemistry Community (C_3P) of the Università degli Studi di Padova are kindly acknowledged.

Notes and references

1 H. B. Gray, J. G. Swanson and T. H. Crawford, *Project Acac*: *An Experimental Investigation in Synthesis and Structure*, Bodgen and Quigley: New York 1972.

2 (a) R. C. Mehrotra, R. Bohra and D. P. Gaur, *Metal β-Diketonates and Allied Derivatives*, Academic Press, London, 1978; (b) R. C. Mehrotra, *Pure Appl. Chem.*, 1988, **35**, 1349.

3 D. P. Craig, *J. Chem. Soc.*, 1951, 3175.

4 (a) F. A. Cotton and G. Wilkinson, *Advanced Inorganic Chemistry* 5th ed., John Wiley & Sons, New York, 1988; (b) N. N. Greenwood and A. Earnshaw, *Chemistry of the Elements*, Butterworth-Heinemann, Cambridge, 2nd edn, 1984.

5 Symmetry properties of $TM(acac)_3$ complexes with O atoms occupying the six vertices of a regular octahedron are described by the D_3 symmetry point group.

6 E. C. Lingafelter, *Coord. Chem. Rev.*, 1966, **1**, 151.

7 The electronic configurations of Cr^{III}, Mn^{III} and Fe^{III} in HS **I**, **II** and **III**, respectively, are: $t_{2g}^3 e_g^0$ with S = 3/2 in **I**, $t_{2g}^3 e_g^1$ with S = 2 in **II**, $t_{2g}^3 e_g^2$ with S = 5/2 in **III** (S corresponds to the total spin angular momentum quantum number).

8 (a) G. C. Levy and R. A. Komoroski, *J. Am. Chem. Soc.*, 1974, **96**, 678; (b) V. I. Vovna and A. I. Streltsov, *J. Struct. Chem.*, 1998, **39**, 917; (c) I. Diaz-Acosta, J. Baker, W. Cordes and P. Pulay, *J. Phys. Chem. A*, 2001, **105**, 238; (d) I. Diaz-Acosta, J. Baker, J. F. Hinton and P. Pulay, *Spectrochim. Acta A*, 2003, **59**, 363; (e) B. Pritchard and J. Autschbach, *Inorg. Chem.*, 2012, **51**, 8340; (f) S. DeBeer George, T. Petrenko and F. Neese, *J. Phys. Chem. A*, 2008, **112**, 12936; (g) R. R. Sharp, *J. Chem. Phys.*, 1993, **98**, 2507; (h) E. C. Wasinger, F. M. de Groot, B. Hedman, K. O. Hodgson and E. I. Solomon, *J. Am. Chem. Soc.* 2003, **125**, 12894; (i) *The Chemistry of Metal Enolates*, Ed. J. Zabicky, John Wiley and Sons, 2009; (j) S. S. Patil, S. V. Patil and V. D. Bobade, *Synlett.*, 2011, 2379.

9 (a) W. S. Rees, *CVD of Nonmetals*, VCH: New York, 1996, (b) T. Kodas and M. Hampden-Smith, *The Chemistry of Metal CVD*, VCH: New York, 1996; (c) *Thin Film Techniques and Applications*, Editors O. N. Sundaram, V. Veeravazhuthi, P. Meena, K. Tamil Selvan, 2004, New Dehli; (d) *Sol-Gel Methods for Materials Processing*, Editors P. Innocenzi, Y. L. Zub and V. G. Kessler, 2008, Springer Science; (e) R. A. Siddiqui, *Experimental Investigations of Thermodynamic Properties of Organometallic Compounds*, TUD*press*, 2010; (f) Y. Xu and X.-T. Yan, *Chemical Vapour Deposition*, An Integrated Engineering Design for Advanced Materials, Springer, London, 2010; (g) B. D. Flockhart and and D. Thorburn Burns, *Pure & Appl. Chem.*, 1987, **59**, 915; (h) A.

N. Kitaigorodskii, A. G. Stepanov and V. M. Nekipelov, *Magn. Res. Chem*., 1986, **24**, 705.

10 More than forty years ago **I** and **III** have been evocatively marked by Levy and Komoroski[8a] as "another powerful weapon in the chemists' arsenal for attacking organic structure problems", being possible alternatives or complements to lanthanide shift reagents in NMR spectroscopy.

11 A. L. Willis, Z. Chen, J. He, Y. Zhu, N. J. Turro and S. O'Brien, *J. Nanomat*., 2007, 14858.

12 K. Chokprasombat, C. Sirisathitkul, P. Harding, S. Chandarak, and R. Yimnirun, *J. Nanomat*., 2012, 758429.

13 F. Pan and Q. Wang, *Molecules*, 2015, **20**, 20499.

14 A. Ejigu, P. A. Greatorex-Davies and D. A. Walsh, *Electrochem. Comm*., 2015, **54**, 55.

15 J. D. Saraidaridis, B. M. Bartlett and C. W. Monroe, *J. Electrochem. Soc.*, 2016, **163**, A1239.

16 Q. Liu, A. A. Shinkle, Y. Li, C. W. Monroe , L. T. Thompson and A. E. S. Sleightholme, *Electrochem. Comm*., 2010, **12**, 1634.

17 (a) E. M. S. Maçoas, R. Kananavicius, P. Myllyperkiö, M. Pettersson and H. Kunttu, *J. Am. Chem. Soc.*, 2007, **129**, 8934, and references therein reported; (b) E. M. S. Maçôas, R. Kananavicius, P. Myllyperkiö, M. Pettersson and H. Kunttu, *J. Phys. Chem. A,* 2007, **111**, 2054; (c) E. M. S. Maçôas, S. Mustalahti, P. Myllyperkiö, H. Kunttu and M. Pettersson, *J. Phys. Chem. A*, 2015, **119**, 2727; (d) E. A. Juban and J. K. McCusker, *J. Am. Chem. Soc*., 2005, **127**, 6857; (e) E. A. Juban, A. L. Smeigh, J. E. Monat and J. McCusker, *Coord. Chem. Rev.*, 2006, **250**, 1783.

18 (a) F. Neese, *J. Am. Chem. Soc.*, 2006, **128**, 10213; (b) A. R. Jaszewski, R. Stranger and R. Pace, *J. Phys. Chem. A*, 2008, **112**, 11223; (c) L. Andjelkovic, M. Gruden-Pavlovic, C. Daul and M. Zlatar, *Int. J. Quantum Chem*., 2013, **113**, 859.

19 (a) J. P. Fackler and A. Avdeef, *Inorg. Chem*. 1974, **13**, 1864; (b) B. R. Stults, R. S. Marianelli and V. W. Day, *Inorg. Chem*. 1979, **18**, 1853; (c) J. Krzystek, G. J. Yeagle, J. H. Park, R. D. Britt, M. W. Meisel, L. C. Brunel and J. Telser, *Inorg. Chem*. 2003, **42**, 4610.

20 R. van Gorkum, E. Bouwman and J. Reedijk, *Inorg. Chem*., 2004, **43**, 2456.

21 J. A. Takacs, G. V. Madhavan, M. Creswell, F. Seely and W. Devroy, *Organometallics*, 1986, **5**, 2395.

22 R. A. Ligabue, A. L. Monteiro, R. F. de Souza and M. O. de Souza, *J. Mol. Cat. A: Chem*., 1998, **130**, 101.

23 A. Sudo, S. Hirayama and T. Endo, *J. Poly. Sci. Poly. Chem*., 2010, **48**, 479.

24 A. Misono, *Bull. Chem. Soc. Jpn.*, 1966, **39**, 2425.

25 K. T. Williamson and T. Yoon, *J. Am. Chem. Soc.*, 2010, **132**, 4570.

26 (a) J. Pinkas, V. Reichlova, R. Zboril, Z. Moravec, P. Bezdicka and J. Matejkova, *Ultrason. Sonochem*., 2008, **15**, 257; (b) T. Hyeon, S. Seong Lee, J. Park, Y. Chung and H. B. Na, *J. Am. Chem. Soc*., 2001, **123**, 12798.

27 I. Rangeeka Perera, T. Daeneke, S. Makuta, Z. Yu, Y. Tachibana, A. Mishra, P. Bäuerle, C. A. Ohlin, U. Bach and L. Spiccia, *Angew. Chem. Int. Ed.*, 2015, **54**, 3758.

28 (a) S. Evans, A. Hamnett, A. F. Orchard and D. R. Lloyd, *Faraday Discuss. Chem. Soc.*, 1972, **54**, 227; (b) H. Van Dam and A. Oskam, *J. Electron. Spectrosc.*, 1979, **17**, 353; (c) M. E. Akopyan, V. I. Vovna, V. I. Kleimenov, S. N. Lopatin and A. Yu. Ustinov, *Opt. Spectrosc. (USSR)*, 1990, **69**, 53; (d) A. Yu. Ustinov, V. I. Vovna and O. M. Ustinova, *J. Electron. Spectrosc.*, 1998, **88-91**, 103; (e) J. B. Westmore, M. L. J. Reimer and C. Reichert, *Can. J. Chem*., 1991, **59**, 1797; (f) V. I. Vovna, I. B. Lvov, Y. V. Ivanov, S. N. Slabzhennikov, A. I. Streltsov and A. Yu. Ustinov, *J. Electron. Spectrosc.*, 1998, **96**, 141.

29 (a) M. M. Conradie, P. H. van Rooyen and J. Conradie, *J. Mol. Struct*., 2013, **1053**, 134; (b) R. Liu and J. Conradie, *Electrochim. Acta*, 2015, **185**, 288.

30 G. L. Miessler, P. J. Fischer and D. A. Tarr, *Inorganic Chemistry*, Pearson, New York, 5th edn, 2013, p. 137.

31 According to their occupation numbers, MOs are divided in doubly occupied MOs (DOMOs), singly occupied MOs (SOMOs) and virtual (empty) MOs (VMOs). Moreover, HOMO and LUMO acronyms stand for highest occupied and lowest unoccupied MO, respectively.

32 (a) A. Bianconi, in *X-ray Absorption: Principles, Applications, Techniques of EXAFS, SEXAFS and XANES*, ed. D. C. Koningsberger and R. Prins, John Wiley & Sons, New York, 1988, pp. 573–662; (b) J. Stöhr, *NEXAFS Spectroscopy*, Springer, Berlin, 1992.

33 H. H. Zhang, B. Hedman and K. O. Hodgson, in *Inorganic Electronic Structure*, ed. E. I. Solomon and A. B. P. Lever, John Wiley & Sons, New York, 1999.

34 E. I. Solomon and C. B. Bell III, in *Physical Inorganic Chemistry, Principle, Methods and Models*, John Wiley & Sons, Hoboken, 2010, pp. 1–37.

35 (a) S. Carlotto, M. Sambi, A. Vittadini and M. Casarin, *Phys. Chem. Chem. Phys.*, 2016, **18**, 2242; (b) S. Carlotto, M. Sambi, A. Vittadini and M. Casarin, *Polyhedron*, 2017, **135**, 216.

36 (a) G. Mangione, L. Pandolfo, M. Sambi, G. Ligorio, M. V. Nardi, A. Cossaro, L. Floreano and M. Casarin, *Eur. J. Inorg. Chem*., 2015, 2707 and references therein reported; (b) M. Rancan, J. Tessarolo, M. Casarin, P. L. Zanonato, S. Quici and L. Armelao, *Inorg. Chem*., 2014, **53**, 7276.

37 The absorption edges are labelled in the order of increasing energy, K, L_1, L_2, L_3, M_1, ..., corresponding to the excitation of an electron from the 1s ($S_{1/2}$), 2s ($S_{1/2}$), 2p ($P_{1/2}$), 2p ($P_{3/2}$), 3s ($S_{1/2}$), ... orbitals (states), respectively.

38 F. Neese, *Wiley Interdiscip. Rev.: Comput. Mol. Sci.*, 2012, **2**, 73.

39 F. Wang, T. Ziegler, E. van Lenthe, S. van Gisbergen and E. J. Baerends, *J. Chem. Phys.*, 2005, **122**, 204103.

40 S. Hirata and M. Head-Gordon, *Chem. Phys. Lett.*, 1999, **314**, 291.

41 (a) E. van Lenthe, E. J. Baerends and J. G. Snijders, *J. Chem. Phys*., 1993, **99**, 4597; (b) E. van Lenthe, E. J. Baerends and J. G. Snijders, *J. Chem. Phys.*, 1994, **101**, 9783; (c) E. van Lenthe, A. Ehlers and E. J. Baerends, *J. Chem. Phys.*, 1999, **110**, 8943.

42 C. K. Jørgensen (*Absorption Spectra and Chemical Bonding in Complexes*, Pergamon Press, Oxford, UK, 1962, p. 77) defined the symmetry-restricted covalency as the effect associated to the dilution, ruled by the complex symmetry, of d orbitals to make them become linear combinations of AOs (LCAO-MOs).

43 H. Ando, S. Iuchi and H. Sato, *Chem. Phys. Lett*., 2012, **535**, 177.

44 Amsterdam Density Functional (ADF) version 2014.01 http://www.scm.com.

45 (a) A. D. Becke, *Phys. Rev. A: At., Mol., Opt. Phys.*, 1988, **38**, 3098; (b) J. P. Perdew, *Phys. Rev. B: Condens. Matter Mater. Phys.*, 1986, **33**, 8822.

46 The high spin TM^{III} electronic configuration is $a^1_{|?|1}e^2e^0$ in **I**, $a^1_{|?|1}e^2e^1$ in **II** and $a^1_{|?|1}e^2e^2$ in **III**. Corresponding ground states (GSs) are $^4A_2$, ^5E, and $^6A_1$, respectively. No Jahn-Teller

distortion[47] is foreseen for **I** and **II** complexes as a consequence of their not orbitally degenerate GSs. Possible Jahn-Teller distortions associated to orbitally degenerate excited states (ES) have not been taken into account.

47 (a) H. A. Jahn and E. Teller, *Proc. R. Soc. London*, 1937, **A161**, 220; (b) H. A. Jahn, *Proc. R. Soc. London*, 1938, **A164**, 117. *Phys.*, 1986, **33**, 8822.

48 R. Hoffmann, *Solids and Surfaces: A Chemist's View of Bonding in Extended Structures*, VCH, New York, 1988.

49 R. S. Mulliken, *J. Chem. Phys.*, 1955, **23**, 1833.

50 T. Ziegler and A Rauk, *Theor. Chim. Acta*, 1977, **46**, 1.

51 ^{TM}K-edge spectral features[37] are generated by the electric dipole forbidden, but quadrupole allowed $1s^{TM} \rightarrow nd^{TM}$ transitions,[52] which may be enhanced in non-centro-symmetric complexes through the involvement of $(n + 1)p^{TM}$ AOs into frontier unoccupied MOs.[53] Differently to that, $^{TM}L_{2,3}$-edges structures[37] are dominated by electric dipole allowed $2p^{TM} \rightarrow nd^{TM}$ transitions,[52,55] which question the contribution of nd^{TM} AOs to the unoccupied electronic structure. At variance to $1s^{TM} \rightarrow nd^{TM}$ transitions, the $2p^6 \rightarrow nd^k$ ones produce a final electronic configuration with a hole in the $2p^{TM}$ core levels ($2p^5nd^{k+1}$) whose orbital angular momentum quantum number ℓ = 1. Spin–orbit coupling (SOC) allows the orbital angular momentum to couple with the spin angular momentum whose quantum number s = 1/2. SOC then generates two distinct states having total angular momentum quantum numbers j = 3/2 and j = 1/2. The former state lies at a lower excitation energy (*EE*) and it corresponds to the L_3 feature,[37] whose intensity is approximately twice the one of the L_2 feature[37] associated to the j = 1/2 state. Both the experimental analysis and the theoretical modelling of $^{TM}L_{2,3}$-edges spectra in TM complexes are challenging issues. In fact, besides ligand-field and covalency effects, the SOC between the numerous possible final-state multiplets has to be taken into account.[56,57] ^{TM}K-edge and $^{TM}L_{2,3}$-edges outcomes of TM complexes may be eventually complemented by L donor atom K-edge (^{O}K-edge in the present case) evidences.[58] As a matter of fact, ^{L}K-edge spectra of TM complexes with partly filled *n*d atomic orbitals (AOs) are usually typified by rather intense pre-edge features generated by the electric dipole allowed[52] $1s^L \rightarrow mp^L$ transitions whose intensity quantifies the participation of the L donor atom *m*p AOs to the unoccupied frontier MOs.[59-61] NEXAFS at the ^{L}K-edge then provides a direct probe of the so-called TM–L symmetry restricted covalency.[42]

52 B. E. Douglas and C. A. Hollingsworth, *Symmetry in Bonding and Spectra, an Introduction*; Academic Press, Inc.: Orlando, 1985; pp 256-257.

53 The ^{M}K-pre-edge is sensitive to 4p-3d mixing on the order of 1%, thus providing a rather accurate estimate of such a mixing.[54]

54 S. DeBeer George, P. Brant and E. I. Solomon, *J. Am. Chem. Soc.*, 2005, **127**, 667.

55 The L_1-edge of the first transition series TM is weak and provides poor spectroscopic information.[56]

56 R. K. Hocking and E. I. Solomon, *Struct. Bonding*, 2012, **142**, 155.

57 (a) F. de Groot, *Coord. Chem. Rev.*, 2005, **249**, 31; (b) F. de Groot and A. Kotani, *Core Level Spectroscopy of Solids*, CRC Press, Boca Raton, 2008; (c) M. Roemelt and F. Neese, *J. Phys. Chem. A*, 2013, **117**, 3069; (d) P. S. Bagus, H. Freund, H. Kuhlenbeck and E. S. Ilton, *Chem. Phys. Lett.*, 2008, **455**, 331; (e) H. Ikeno, T. Mizoguchi and I. Tanaka, *Phys. Rev. B: Condens. Matter Mater. Phys.*, 2011, **83**, 155107; (f) I. Josefsson, K. Kunnus, S. Schreck, A. Föhlisch, F. de Groot, P. Wernet and M. Odelius, *J. Phys. Chem. Lett.*, 2012, **3**, 3565; (g) D. Maganas, M. Roemelt, M. Hävecker, A. Trunschke, A. Knop-Gericke, R. Schlögl and F. Neese, *Phys. Chem. Chem. Phys.*, 2013, **15**, 7260; (h) M. Roemelt, D. Maganas, S. DeBeer and F. Neese, *J. Chem. Phys.*, 2013, **138**, 204101; (i) D. Maganas, S. DeBeer and F. Neese, *Inorg. Chem.*, 2014, **53**, 6374; (j) D. Maganas, M. Roemelt, T. Weyhermüller, R. Blume, M. Hävecker, A. Knop-Gericke, S. DeBeer, R. Schlögl and F. Neese, *Phys. Chem. Chem. Phys.*, 2014, **16**, 264.

58 (a) B. Hedman, K. O. Hodgson and E. I. Solomon, *J. Am. Chem. Soc.*, 1990, **112**, 1643; (b) S. E. Shadle, B. Hedman, K. O. Hodgson and E. I. Solomon, *Inorg. Chem.*, 1994, **33**, 4235; (c) S. E. Shadle, B.Hedman, K. O. Hodgson and E. I. Solomon, *J. Am. Chem. Soc.*, 1995, **117**, 7; (d) F. Neese, B. Hedman, K. O. Hodgson and E. I. Solomon, *Inorg. Chem.*, 1999, **38**, 4854.

59 The higher the intensity, the higher the contribution of the L donor atoms to the unoccupied frontier MOs and, accordingly, the M–L covalent character.

60 T. Glaser, B. Hedman, K. O. Hodgson and E. I. Solomon, *Acc. Chem. Res.*, 2000, **33**, 859.

61 E. I. Solomon, B. Hedman, K. O. Hodgson, A. Deya and R. K. Szilagyic, *Coord. Chem. Rev.*, 2005, **249**, 97.

62 In a TM *octahedral* environment, the linear combinations of the six $1s^O$ AOs transform as the $a_{1g} + e_g + t_{1u}$ irreducible representations (IRs) of the O_h symmetry point group. The $O_h \rightarrow D_3$ descending symmetry implies the following correlations $a_{1g} \rightarrow a_1$; $e_g \rightarrow e$; $t_{1u} \rightarrow a_2 + e$.[52]

63 (a) G. Fronzoni, M. Stener, P. Decleva, F. Wang, T. Ziegler, E. van Lenthe and E. J. Baerends, *Chem. Phys. Lett.*, 2005, **416**, 56; (b) G. Fronzoni, M. Stener, P. Decleva, M. De Simone, M. Coreno, P. Franceschi, C. Furlani and K. C. Prince, *J. Phys. Chem. A*, 2009, **113**, 2914; (c) M. Casarin, P. Finetti, A. Vittadini, F. Wang and T. Ziegler, *J. Chem. Phys. A*, 2007, **111**, 5270; (d) M. V. Nardi, R. Verucchi, L. Pasquali, G. Fronzoni, M. Sambi, G. Mangione and M Casarin, *Phys. Chem. Chem. Phys.*, 2015, **17**, 2001; (e) M. V. Nardi, F. Detto, L. Aversa, R. Verucchi, G. Salviati, S. Iannotta and M. Casarin, *Phys. Chem. Chem. Phys.*, 2013, **15**, 12864; (f) G. Mangione, S. Carlotto, M. Sambi, G. Ligorio, M. Timpel, A. Vittadini, M. V. Nardi and M Casarin, *Phys. Chem. Chem. Phys.*, 2016, **18**, 18727; (g) G. Mangione, M. Sambi, S. Carlotto, A. Vittadini, G. Ligorio, M. Timpel, L. Pasquali, A. Giglia, M. V. Nardi and M Casarin, *Phys. Chem. Chem. Phys.*, 2016, **18**, 24890.

64 E. van Lenthe and E. J. Baerends, *J. Comput. Chem.*, 2003, **24**, 1142.

65 E. K. U. Gross and W. Kohn, *Adv. Quantum Chem.*, 1990, **21**, 255.

66 C. Adamo and V. Barone, *J. Chem. Phys.*, 1999, **110**, 6158.

67 O. V. Gritsenko, P. R. T. Schipper and E. J. Baerends, *Chem. Phys. Lett.*, 1999, **302**, 199.

68 R. van Leeuwen and E. J. Baerends, *Phys. Rev.* A, 1994, **49**, 2421.

69 (a) Y. Zhao and D. G. Truhlar, *J. Chem. Phys.*, 2006, **125**, 194101; (b) Y. Zhao and D. G. Truhlar, *Theor. Chem. Acc.*, 2008, **120**, 215.

70 PBE0,[66] SAOP,[67] LB94,[68] and M06[69] numerical experiments have been carried out by using the NR BP86[45] optimized geometries.

71 J. H. van Lenthe, S. Faas and J. G. Snijders, *Chem. Phys. Lett.*, 2000, **328**, 107.

72 (a) F. Weigend and R. Ahlrichs, *Phys. Chem. Chem. Phys.*, 2005, **7**, 3297; (b) F. Weigend, *Phys. Chem. Chem. Phys.*, 2006, **8**, 1057.

73 A detailed description of basis sets' acronyms is reported in the ORCA manual (https://orcaforum.cec.mpg.de/).

74 (a) E. J. Baerends, D. E. Ellis and P. Ros, *Chem. Phys.*, 1973, **2**, 41; (b) B. I. Dunlap, J. W. D. Connolly and J. R. Sabin, *J. Chem. Phys.*, 1979, **71**, 3396; (c) C. Van Alsenoy, *J. Comput. Chem.*, 1988, **9**, 620.

75 V. I. Lebedev, *Zh. Vychisl. Mat. Fiz.*, 1975, **15**, 48.

76 D. Coster and R. D. L. Kronig, *Physica*, 1935, **2**, 13.

77 L. Floreano, A. Cossaro, R. Gotter, A. Verdini, G. Bavdek, F. Evangelista, A. Ruocco, A. Morgante and D. Cvetko, *J. Phys. Chem. C*, 2008, **112**, 10794.

78 L. Floreano, G. Naletto, D. Cvetko, R. Gotter, M. Malvezzi, L. Marassi, A. Morgante, A. Santaniello, A. Verdini, F. Tommasini and G. Tondello, *Rev. Sci. Instrum.*, 1999, **70**, 3855.

79 C. Glidewell in *Inorganic Experiments, Third Edition*, ed. D. Woolins, Wiley-VCH: Weinheim, Germany, 2010; p 109.

80 Unoccupied frontier orbitals may correspond to final spin orbitals – fsos – in ^{O}K-edge and $^{TM}L_{2,3}$-edges NEXAFS transitions.

81 F. D. Lewis, G. D. Salvi, D. R. Kanis and M. A. Ratner, *Inorg. Chem.*, 1993, **32**, 1251.

82 In the adopted framework, $^{e}t_{2g}$ ($^{a}t_{2g}$) orbitals correspond to the $x^2 - y^2$ and xy (z^2) TM 3d AOs, while the e_g-like ones are the xz and yz TM 3d AOs. The TM $^{a}t_{2g}$ AO may only interact with the a_1 linear combinations of the L-based n_+ and π_e orbitals. Both the localization and the relative energy position of the occupied (unoccupied) acac-based π_2 (π_4) FMO[81] concur to foresee negligible the interaction between them and the $^{a}t_{2g}$ AO.

83 The HS electronic configurations $a_1^1e^2e^0$, $a_1^1e^2e^1$ and $a_1^1e^2e^2$ are obviously reminiscent of the HS $t_{2g}^3e_g^0$, $t_{2g}^3e_g^1$ and $t_{2g}^3e_g^2$ ones, respectively.

84 Throughout the paper, the MO numbering is the one corresponding to the all-electron calculations independently of the adoption of the frozen core approximation.

85 Spin ↑ COOPs between TM^{III} t_{2g}-like 3d AOs and linear combinations of $(acac)_3^{3-}$-based π_4 FMOs, not herein reported, testifies the absence of any TM^{III} → L backbonding.

86 B. Pritchard and J. Autschbach, *Inorg. Chem.*, 2012, **51**, 8340.

87 The quasi degenerate $(acac)_3^{3-}$-based 28e(↑) and 28e(↓) orbitals have the same Cr–O bonding character (see Fig. S2 of the ESI†).

88 (a) R. F. Nalewajski and J. Mrozek, *Int. J. Quantum Chem.*, 1994, **51**, 187; (b) R. F. Nalewajski, J. Mrozek, S. J. Formosinho and A. J. C. Varandas, *Int. J. Quantum Chem.*, 1994, **52**, 1153; (c) R. F. Nalewajski and J. Mrozek, *Int. J. Quantum Chem.*, 1996, **57**, 377; R. F. Nalewajski, J. Mrozek and G. Mazur, *Can. J. Chem.*, 1996, **74**, 1121; (d) R. F. Nalewajski, J. Mrozek and A. Michalak, *Int. J. Quantum Chem.*, 1997, **61**, 589; (e) R. F. Nalewajski, J. Mrozek and A. Michalak, *Pol. J. Chem.*, 1998, **72**, 1779.

89 I^{NM} includes both covalent and ionic contributions.[88]

90 F. L. Hirshfeld, *Theor. Chim. Acta*, 1977, **44**, 129.

91 C. Fonseca Guerra, J.-W. Handgraaf, E. J. Baerends and F. M. Bickelhaupt, *J. Comput. Chem.*, 2004, **25**, 189.

92 In $Al(acac)_3$, the arrangement of the acac fragments about the 3d-electron free Al^{III} ion reproduces the one characterizing **I**, **II**, and **III**. BP86 calculations pertaining to the optimized $Al(acac)_3$ provide the following I^{NM}, $Q^{Al}_{Hir}/Q^{Al}_{Vor}$ and Q^{O}_{Hir}/Q^{O}_{Vor} values: 0.49, 0.44/0.36 and -0.20/ -0.20, respectively.

93 (a) J. W. Rabalais, *Principle of Ultravioled Photoelectron Spectroscopy,* J. Wiley and Sons, New York, 1977; (b) R. G. Egdell and A. W Potts in *Electronic structure and magnetism of inorganic compounds*, Chemical Society. Specialist periodical reports, 1980, **6**, 1; (c) R. G. Egdell in *Electronic structure and magnetism of inorganic compounds*, Chemical Society. Specialist periodical reports, 1982, **7**, 1.

94 Evans *et al.*[28a] report in their contribution the vapour-phase He(I) PE spectra for a quite large number of β-diketonate ML_3 complexes (L = hexafluoroacac (hfa), trifluoroacac and acac; M = Al, Ga, Sc, Ti, V, Cr, Co, Mn, Fe, Ru). The $Mn(hfa)_3$ He(I) PE spectrum is presented by the authors (Fig. 15 of the ref. 28a), while the opposite is true for the $Mn(acac)_3$ one. Nevertheless, the IEs of the $Mn(acac)_3$ lowest lying PE features (an almost imperceptible shoulder at 7.32 eV followed by a band at 8.14 eV) are collected with data pertaining to $Mn(hfa)_3$ in the Table 6 of the ref. 28a.

95 The $M(hfa)_3$ PE spectra (M = Al, Cr, Fe)[28,96] are very similar to the $M(acac)_3$ ones,[28] with the $M(hfa)_3$ spectral patterns uniformly blue-shifted by ~ 2 eV with respect to the $M(acac)_3$ ones. A rough estimate of the ^{II}IEs can be then obtained by referring to the $Mn(hfa)_3$ spectrum[28a] and applying a red-shift of 2 eV.

96 D. R. Lloyd, *Chem. Commun.*, 1970, 868.

97 The wavelength (energy) of the He(I) and He(II) ionizing sources amounts to 584 (21.22 eV) and 304 Å (40.81 eV), respectively.[93]

98 U. Gelius, in *Electron Spectroscopy*, ed. D. A. Shirley, North-Holland, Amsterdam, 1972, p. 311.

99 A. Berndtsson, E. Basilier, U. Gelius, J. Hedman, M. Klasson, R. Nilsson, C. Nordling and S. Svensson, *Phys. Scr.*, 1975, **12**, 235.

100 $(\sigma_{2p}^{C})^{He(II)}/(\sigma_{2p}^{C})^{He(I)}$, $(\sigma_{2p}^{O})^{He(II)}/(\sigma_{2p}^{O})^{He(I)}$ and $(\sigma_{3d}^{TM})^{He(II)}/(\sigma_{3d}^{TM})^{He(I)}$ ASPCS ratios amount to 3.06×10^{-1}, 6.39×10^{-1}, and 9.25×10^{-1} (Cr), 1.56 (Mn), 1.81 (Fe).[101]

101 J. J. Yeh and I. Lindau, *At. Data Nucl. Data Tables*, 1985, **32**, 1.

102 J. C. Slater, *Quantum Theory of Molecules and Solids. The Self-Consistent-Field for Molecules and Solids*, McGraw-Hill, New York, 1974, vol. 4.

103 The same assignment has been proposed by Vovna *et al.*[28f] despite the GS topmost lying orbitals they evaluated by means of Hartree-Fock-Slater discrete variational Xα calculations[104] did not include any Cr^{III} 3d-based MOs.

104 (a) D. E. Ellis and G. S. Painter, *Phys. Rev. B Solid State*, 1970, **2**, 2887; (b) F. W. Averill and D. E. Ellis, *J. Chem. Phys*., 1973, **59**, 6412; (c) E. J. Baerends, D. E. Ellis and P. Ros, *Chem. Phys.*, 1973, **2**, 41; (d) A. Rosen, D. E. Ellis, H. Adachi and F. W. Averill, *J. Chem. Phys.*, 1976, **65**, 3329; (e) B. Delley and D. E. Ellis, *J. Chem. Phys.*, 1982, **76**, 1949.

105 Similar considerations hold for $Ti(acac)_3$ and $V(acac)_3$ (see Fig. 1 of the ref. 28f).

106 The participation of the Mn-based e_g-like and $^{e}t_{2g}$ orbitals to the 94a(↑) HOMO (95a(↑) LUMO)[84] amounts to 32 and 17% (33 and 23%), respectively.

107 In the ^{Z}TS scheme,[50] the bonding energy (BE) may be written as the sum of contributions due to the steric repulsion (ΔE_{ster}, a positive quantity), in turn equal to the pure electrostatic interaction plus the Pauli repulsion, the orbital interaction (ΔE_{int}, a negative quantity) and, eventually, the so-called preparation energy and the basis set superposition error.

108 S. Evans, A. Hamnett and A. F. Orchard, *Chem. Commun*., 1970, 1282.

109 The $Fe(hfa)_3$ vapour-phase He(I) PE spectrum[96] is characterized by a very low intensity band at 8.28 eV that Lloyd[96] assigned to the ionization from the Fe^{III} e_g-like orbitals; Evans *et al.*[108] suggested an alternative assignment for the same PE feature: "… a shadow, excited by an additional line at 23.09 eV in the helium source, of the prominent PE band A."

110 F. Wang and T. Ziegler, *Mol. Phys.*, 2004, **102**, 2585.

111 $Mn(acac)_3$ $1s^{O}$-based orbitals correspond to the 6a – 11a DOMOs.

112 Atomic multiplets associated to the presence of four/six[113] (five) electrons in the 3d AOs are: ^{5}D, ^{3}H, ^{3}G, $^3F_{\pm}$, ^{3}D, $^3P_{\pm}$, ^{1}I, $^1G_{\pm}$, ^{1}F, $^1D_{\pm}$, $^1S_{\pm}$ (^{6}S, ^{4}G, ^{4}F, ^{4}D, ^{4}P, ^{2}I, ^{2}H, $2 \times {}^2$G, $2 \times {}^2$F, ^{2}D, $^2D_{\pm}$, ^{2}P, ^{2}S) for a total of 210 (252) microstates.[115] The number of final state pure spin-functions that can be formed from the $2p^53d^{4/6}$ and $2p^53d^5$ configurations are 450 and 600, respectively.

113 "… terms arising from n (<5) d electrons outside an argon shell are the same as those arising from 10 – n electrons outside the same shell or, equivalently, of n holes in the completed d^{10} shell."[114]

114 C. J. Ballhausen, *Introduction to Ligand Field Theory*, McGrow-Hill Book Company, Inc., New York, 1962, p. 69

115 The interested reader may refer to Table 4.8 of ref. 116.

116 F. de Groot and A. Kotani, *Core Level Spectroscopy of Solids*, CRC Press, Boca Raton, 2008.

117 The $\Delta S = 0$ spin-selection rule is slightly released when SOC is considered. More specifically, SOC connects the terms with resultant spins S and S', where $|S - S'| = 0, 1$.[118]

118 S. Sugano, Y. Tanabe and H. Kamimura, Multiplets of Transition-Metal Ions in Crystals, 1970, Academic Press, New York.

119 S. Carlotto, M. Sambi, F. Sedona, A. Vittadini, J. Bartolomé, F. Bartolomé and M. Casarin, *Phys. Chem. Chem. Phys.*, 2016, **18**, 28110.

120 M. M. Grush, Y. Muramatsu, J. H. Underwood, E. M. Gullikson, D. L. Ederer, R. C. C. Perera and T. A. Callcott, *J. Electron. Spectrosc. Relat. Phenom.*, 1998, **92**, 22.

121 The inspection of Fig. 10 reveals that the $^{II}L_2{}^1$ and $^{II}L_2{}^2$ relative positions agree well with experimental evidences but their relative intensities are opposite to the experimental ones.